The Astrophysical Journal, 880:129 (21pp), 2019 August 1 https://doi.org/10.3847/1538-4357/ab2adc

New Analytic Solutions for Galaxy Evolution: Gas, Stars, Metals, and Dust in Local ETGs and Their High-z Star-forming Progenitors

L. Pantoni[1], A. Lapi[1,2,3,4], M. Massardi[5], S. Goswami[1], and L. Danese[1,2]
[1] SISSA, Via Bonomea 265, I-34136 Trieste, Italy
[2] IFPU—Institute for Fundamental Physics of the Universe, Via Beirut 2, I-34014 Trieste, Italy
[3] INFN–Sezione di Trieste, via Valerio 2, I-34127 Trieste, Italy
[4] INAF–Osservatorio Astronomico di Trieste, via Tiepolo 11, I-34131 Trieste, Italy
[5] INAF, Istituto di Radioastronomia—Italian ARC, Via Piero Gobetti 101, I-40129 Bologna, Italy
Received 2019 April 8; revised 2019 May 30; accepted 2019 June 17; published 2019 August 2

Abstract

We present a set of new analytic solutions aimed at self-consistently describing the spatially averaged time evolution of the gas, stellar, metal, and dust content in an individual star-forming galaxy hosted within a dark halo of a given mass and formation redshift. Then, as an application, we show that our solutions, when coupled to specific prescriptions for parameter setting (inspired by in situ galaxy–black hole coevolution scenarios) and merger rates (based on numerical simulations), can be exploited to reproduce the main statistical relationships followed by early-type galaxies and their high-redshift star-forming progenitors. Our analytic solutions allow one to easily disentangle the diverse role of the main physical processes regulating galaxy formation, quickly explore the related parameter space, and make transparent predictions on spatially averaged quantities. As such, our analytic solutions may provide a basis for improving the (subgrid) physical recipes presently implemented in theoretical approaches and numerical simulations and can offer a benchmark for interpreting and forecasting current and future broadband observations of high-redshift star-forming galaxies.

Key words: dust, extinction – evolution – galaxies: abundances – galaxies: evolution – galaxies: formation – galaxies: high-redshift

1. Introduction

Understanding the formation and evolution of galaxies in a cosmological context is one of the main challenges of modern astrophysics (e.g., Mo et al. 2010; Silk & Mamon 2012; Maiolino & Mannucci 2019). The issue is intrinsically very complex, since it involves many physical processes occurring on vastly different spatial, time, and energy scales.

The ultimate approach to address the problem in fine detail would require the exploitation of intensive hydrodynamical simulations (e.g., Bekki 2013, 2015; Dubois et al. 2014, 2016; Genel et al. 2014; Hopkins et al. 2014, 2018; Vogelsberger et al. 2014; Schaye et al. 2015; McAlpine et al. 2016, 2019; Zhukovska et al. 2016; Aoyama et al. 2017, 2018; McKinnon et al. 2017, 2018; Pallottini et al. 2017; Torrey et al. 2019; Springel et al. 2018; Ricarte et al. 2019; for a review and further references, see Naab & Ostriker 2017). However, despite the considerable increase in resolution achieved recently, many of the physical processes relevant to the description of galaxy evolution constitute subgrid physics and must be modeled via parametric recipes; in addition, a detailed exploration of the related parameter space or different modeling prescriptions is often limited by exceedingly long computational times.

An alternative route to investigate the issue relies on semi-analytic models (e.g., Kauffmann et al. 1993; Lacey & Cole 1993; Cole et al. 2000; De Lucia et al. 2014, 2017; Croton et al. 2006; Somerville et al. 2008; Arrigoni et al. 2010; Benson 2012; Porter et al. 2014; Cousin et al. 2016; Hirschmann et al. 2016; Lacey et al. 2016; Fontanot et al. 2017; Popping et al. 2017; Collacchioni et al. 2018; Lagos et al. 2018; Forbes et al. 2019; for a review and further references, see Somerville & Dave 2015). These are based on dark matter merger trees extracted from or gauged on N-body simulations, while the physics relevant for galaxy evolution inside dark halos is modeled via several parametric expressions partly set on a number of (mainly local) observables. Such models are less computationally expensive than hydrodynamic simulations and allow one to more clearly disentangle the relative role of the various physical processes at work; however, the considerable number of fudge parameters can lead to degenerate solutions and somewhat limit the predictive power, especially toward high redshift.

Finally, some specific issues related to the global evolution of the baryonic content in galaxies can be tackled with analytic models, i.e., models with analytic solutions (e.g., Schmidt 1963; Talbot & Arnett 1971; Tinsley 1974; Pagel & Patchett 1975; Hartwick 1976; Chiosi 1980; Matteucci & Greggio 1986; Edmunds 1990; Dwek 1998; Hirashita 2000, Hirashita et al. 2015; Chiappini et al. 2001; Draine 2003, 2011; Inoue et al. 2003; Greggio 2005; Naab & Ostriker 2006; Erb 2008; Zhukovska et al. 2008; Valiante et al. 2009; Bouche et al. 2010; Dwek & Cherchneff 2011; Davé et al. 2012; Asano et al. 2013; Lilly et al. 2013; de Bennassuti et al. 2014; Dekel & Mandelker 2014; Forbes et al. 2014a; Pipino et al. 2014; Feldmann 2015; Mancini et al. 2015; Mollá et al. 2015; Recchi & Kroupa 2015; Rodriguez-Puebla et al. 2016; Andrews et al. 2017; Gioannini et al. 2017; Spitoni et al. 2017; Vincenzo et al. 2017; Weinberg et al. 2017; Grisoni et al. 2018; Imara et al. 2018; Tacchella et al. 2018a; Dekel et al. 2019; for a review and further references, see Matteucci 2012). These are necessarily based on approximate and spatially/time-averaged descriptions of the most relevant astrophysical processes; however, the transparent, handy, and predictive character of analytic solutions often pays off.

In the present paper, we develop a set of new analytic solutions aimed at describing the spatially averaged time evolution of the gas, stellar, metal, and dust content in an

individual star-forming galaxy hosted within a dark halo of given mass and formation redshift. Our basic framework pictures a galaxy as an open, one-zone system comprising three interlinked mass components: a reservoir of warm gas subject to cooling and condensation toward the central regions, cold gas fed by infall and depleted by star formation and stellar feedback (Type II supernovae (SNe) and stellar winds), and stellar mass, partially restituted to the cold phase by stars during their evolution. Remarkably, the corresponding analytic solutions for the metal enrichment history of the cold gas and stellar mass are self-consistently derived, using as input the solutions for the evolution of the mass components; the metal equations include the effects of feedback, astration, instantaneous production during star formation, and delayed production by Type Ia SNe, possibly following a specified delay-time distribution (DTD). Finally, the dust mass evolution takes into account the formation of grain cores associated with star formation and grain mantles due to accretion onto preexisting cores; astration of dust by star formation and stellar feedback and spallation by SN shock waves are also included.

We then apply our analytic solutions to describe the formation of spheroids/early-type galaxies (ETGs) and the evolution of their star-forming progenitors. To this purpose, we couple our solutions to two additional ingredients: (i) specific prescriptions for parameter setting, inspired by in situ galaxy–black hole (BH) coevolution scenarios of ETG formation, and (ii) estimates of the halo and stellar mass growth by mergers, computed on the basis of the merger rates from state-of-the-art numerical simulations. We then derive and confront with available data a bunch of fundamental spatially averaged quantities: the star formation efficiency, star formation rate (SFR), gas mass, gas metallicity, stellar metallicity, [α/Fe] ratio, dust mass, and outflowing gas metallicity as a function of the observed stellar mass.

The paper is organized as follows. In Section 2 we present new analytic solutions for the time evolution of the gas and stellar masses (Section 2.1), metals (Section 2.2), dust (Section 2.3), and outflowing matter (Section 2.4); our solutions are compared with classic analytic models in the Appendix. In Section 3 we apply our solutions to high-redshift star-forming galaxies. We first provide physical prescriptions to set the parameters' ruling infall and star formation (Section 3.1), feedback (Section 3.2), and metal and dust production/restitution (Section 3.3); we then discuss how to include the halo and stellar mass growth after formation (Section 3.4) and compute observable quantities at a given observation redshift by averaging over different formation redshifts (Section 3.5). In Section 4 we present a comparison between our results and available observations concerning the evolution of individual galaxies (Section 4.1), the star formation efficiency (Section 4.2), the galaxy main sequence (MS; Section 4.3), the gas mass (Section 4.4), the dust mass (Section 4.5), the gas metallicity (Section 4.6), the stellar metallicity and α-enhancement (Section 4.7), and the outflowing gas metallicity (Section 4.8). In Section 5 we summarize our approach and main findings.

Throughout this work, we adopt the standard flat ΛCDM cosmology (Planck Collaboration 2018) with rounded parameter values: matter density $\Omega_M = 0.32$, dark energy density $\Omega_\Lambda = 0.63$, baryon density $\Omega_b = 0.05$, Hubble constant $H_0 = 100\,h$ km s^{-1} Mpc^{-1} with $h = 0.67$, and mass variance $\sigma_8 = 0.81$ on a scale of $8\,h^{-1}$ Mpc. In addition, we use the widely adopted Chabrier (2003, 2005) initial mass function (IMF) with shape $\phi(\log m_\star) \propto \exp[-(\log m_\star - \log 0.2)^2/2 \times 0.55^2]$ for $m_\star \lesssim 1\,M_\odot$ and $\phi(\log m_\star) \propto m_\star^{-1.35}$ for $m_\star \gtrsim 1\,M_\odot$, continuously joint at $1\,M_\odot$ and normalized as $\int_{0.1\,M_\odot}^{100\,M_\odot} dm_\star m_\star \phi(m_\star) = 1\,M_\odot$. Finally, a value of $Z_\odot \approx 0.014$ for the solar metallicity is adopted, corresponding to $12 + \log[\mathrm{O/H}]_\odot = 8.69$ (see Allende Prieto et al. 2001).

2. Analytic Solutions for Individual Galaxies

In this section, we present new analytic solutions for the time evolution of the mass, metal, and dust components in high-z star-forming galaxies, in particular in the progenitors of ETGs. These are derived from a quite general framework, meant to capture the main physical processes regulating galaxy formation on a spatially averaged ground. The most relevant solutions are highlighted with a box; a comparison of these with classic analytic models, like the closed/leaky box and gas regulator, is provided in the Appendix.

2.1. Gas and Stars

We consider a one-zone description of a galaxy with three interlinked mass components: the infalling gas mass $M_{\rm inf}$, cold gas mass $M_{\rm cold}$, and stellar mass $M_\star$. The evolution of these components is described by the following system of ordinary differential equations:

$$\begin{cases} \dot{M}_{\rm inf} = -\dfrac{M_{\rm inf}}{\tau_{\rm cond}}, \\ \dot{M}_\star = \dfrac{M_{\rm cold}}{\tau_\star}, \\ \dot{M}_{\rm cold} = \dot{M}_{\rm inf} - \gamma\,\dot{M}_\star, \end{cases} \tag{1}$$

where $\gamma \equiv 1 - \mathcal{R} + \epsilon_{\rm out}$. These equations prescribe that the infalling gas mass $M_{\rm inf}$ cools and condenses into the cold gas phase $M_{\rm cold}$ over a characteristic timescale $\tau_{\rm cond}$; then the stellar mass $M_\star$ is formed from the cold mass $M_{\rm cold}$ at a rate $\dot{M}_\star$ over a characteristic timescale $\tau_\star = \tau_{\rm cond}/s$. The cold gas mass is further replenished at a rate $\mathcal{R}\,\dot{M}_\star$ by stellar recycling, where $\mathcal{R}$ is the return fraction of gaseous material from stellar evolution, and it is removed at a rate $\epsilon_{\rm out}\,\dot{M}_\star$ by outflows driven from Type II SN explosions and stellar winds, where $\epsilon_{\rm out}$ is the mass loading factor. Note that in Equation (1), the quantity $M_\star(\tau) \equiv \int_0^\tau d\tau' \dot{M}_\star(\tau')$ represents the integral of the SFR over the galactic age, while the true relic stellar mass after the loss due to stellar evolution is $M_\star^{\rm relic} \simeq (1 - \mathcal{R}) M_\star$. We adopt an IMF $\phi(m_\star)$ uniform in space and constant in time and assume the instantaneous mixing (gas is well mixed at any time) and recycling (stars with mass $m_\star \gtrsim 1\,M_\odot$ die as soon as they form, while those with $m_\star \lesssim 1\,M_\odot$ live forever) approximations, so that the recycled fraction (fraction of a stellar population not locked into long-living dark remnants) can be computed as

$$\mathcal{R} \equiv \int_{1\,M_\odot}^{100\,M_\odot} dm_\star (m_\star - m_{\rm rem})\,\phi(m_\star), \tag{2}$$

where $m_{\rm rem}(m_\star)$ is the mass of the remnants; for our fiducial Chabrier (2003, 2005) IMF, the recycling fraction amounts to $\mathcal{R} \approx 0.45$. Standard initial conditions for the above system of equations read $M_{\rm inf}(0) = f_{\rm inf}\,M_b$ and $M_{\rm cold}(0) = M_\star(0) = 0$; here $M_b = f_b\,M_{\rm H}$ is the baryonic mass originally present in the

host halo with mass $M_{\rm H}$, while $f_{\rm inf} = M_{\rm inf}/f_{\rm b}\,M_{\rm H}$ is the fraction of such a mass that can effectively cool and inflow toward the inner regions of the halo over the timescale $\tau_{\rm cond}$. We will discuss prescriptions for setting these parameters, apt for high-z star-forming galaxies and in particular for ETG progenitors, in Section 3; for the reader's convenience, we anticipate here that typical values for a halo with mass $M_{\rm H} \approx 10^{12}\,M_{\odot}$ formed at $z_{\rm form} \approx 2$ turn out to be $\tau_{\rm cond} \approx$ a few 10^8 yr, $s \approx 3$, $f_{\rm inf} \lesssim 1$, and $\epsilon_{\rm out} \lesssim 2$.

A few caveats on the general structure of Equation (1) are in order. First, with our main focus being to derive analytic solutions for high-redshift star-forming galaxies, particularly for the progenitors of local spheroids/ETGs, we have not included in the equations above a number of processes that can be otherwise relevant for the evolution of local disk-dominated/spiral galaxies, such as galactic fountains and radial gas flows (e.g., Bregman 1980; Lacey & Fall 1985; Pitts & Tayler 1989; Spitoni et al. 2008, 2013; Fu et al. 2013; Forbes et al. 2014b; Pezzulli & Fraternali 2016; Stevens et al. 2016, 2018; Stevens & Brown 2017), differential galactic winds (e.g., Pilyugin 1993; Marconi et al. 1994; Recchi et al. 2008), and multizonal structures and stellar mixing (see Kubryk et al. 2015; Spitoni et al. 2015; Grisoni et al. 2018).

Second, as will be discussed in Section 3.2, the star formation timescale and the duration of the main star formation episode in high $z \gtrsim 1$ star-forming galaxies, particularly ETG progenitors, are typically of order from a few 10^8 to 10^9 yr (e.g., Thomas et al. 2005; Gallazzi et al. 2006, 2014); moreover, most of the star formation process occurs in a central compact region of size around a few kpc (e.g., Scoville et al. 2014, 2016; Ikarashi et al. 2015; Simpson et al. 2015; Straatman et al. 2015; Spilker et al. 2016; Tadaki et al. 2017a, 2017b; Lang et al. 2019). Given that, one can safely neglect in Equation (1) additional terms describing the growth of the host dark matter halo and the stellar content due to accretion and/or mergers that typically occur over cosmological timescales of several Gyr and large spatial scales of order from several tens of kpc (stellar mass addition by galaxy mergers) to several hundred kpc (growth of dark matter (DM) halo and gaseous baryon reservoir); nonetheless, these mass additions will become relevant in the long-term evolution of ETG progenitors toward the present and will be included in our computations, as detailed in Section 3.4.

Third, note that a classic way to link the SFR and the cold gas mass, adopted by many analytic models focused on disk galaxies, is the classic Schmidt–Kennicutt (Schmidt 1959; Kennicutt 1998) law; this prescribes $\dot{\Sigma}_{\star} \propto \Sigma_{\rm cold}^{1.4}$ in terms of the stellar and gas disk surface densities $\Sigma_{\star}$ and $\Sigma_{\rm cold}$. However, in the equations above, we have instead adopted a spatially averaged star formation law $\dot{M}_{\star} \propto M_{\rm cold}$ linearly linking the SFR and the total cold gas mass; this is indicated by recent observations of local starbursts and high-redshift $z \gtrsim 1$ star-forming galaxies (see Krumholz et al. 2012; Scoville et al. 2016, 2017) and is also suggested for local disk galaxies by spatially resolved observations of dense gas in molecular clouds (e.g., Bigiel et al. 2008; Lada et al. 2010). We further note that the star formation law $\dot{M}_{\star} = M_{\rm cold}/\tau_{\star}$ has been written in terms of the total cold gas mass, but it can be equivalently expressed as $\dot{M}_{\star} = f_{\rm H2}\,M_{\rm cold}/\tau_{\star,{\rm H2}}$ in terms of the molecular gas fraction $f_{\rm H2}$ by simply redefining the star formation timescale $\tau_{\star} = \tau_{\star,{\rm H2}}/f_{\rm H2}$ (see Feldmann 2015).

The above system of linear equations can be easily solved analytically in the form

$$\begin{cases} M_{\rm inf}(x) = f_{\rm inf}\,M_{\rm b}\,e^{-x}, \\ M_{\rm cold}(x) = \dfrac{f_{\rm inf}\,M_{\rm b}}{s\,\gamma - 1}[e^{-x} - e^{-s\,\gamma\,x}], \\ M_{\star}(x) = \dfrac{f_{\rm inf}\,M_{\rm b}\,s}{s\,\gamma - 1}\left[1 - e^{-x} - \dfrac{1}{s\,\gamma}(1 - e^{-s\,\gamma\,x})\right], \end{cases} \tag{3}$$

where $x \equiv \tau/\tau_{\rm cond}$ is a dimensionless time variable normalized to the condensation timescale, and $s \equiv \tau_{\rm cond}/\tau_{\star}$ is the ratio between the condensation and star formation timescales. Note that the above solution is physically meaningful (specifically, the cold and stellar masses are nonnegative for any x) whenever $s\gamma > 1$. Since $1/\gamma = 1/(1 - \mathcal{R} + \epsilon_{\rm out}) \lesssim 1/(1 - \mathcal{R}) \lesssim 2$, it is sufficient that $s \gtrsim 2$; as will be discussed in Sections 3.1–3.2 and shown in Figure 1, for ETG progenitors, typical values $s \gtrsim 3$ apply at any mass and redshift, so that the above condition is regularly met. In a nutshell, according to Equation (3), the infalling gas mass declines exponentially with time, while the cold gas mass (hence the SFR) features initial growth, then attains a maximum and eventually declines exponentially. Our analytic solution for the gas mass is compared with that from classic analytic models in the Appendix.

It is instructive to examine the initial behavior of the solutions for $\tau \ll \tau_{\rm cond}$, which read

$$\begin{cases} M_{\rm inf} \simeq f_{\rm inf}\,M_{\rm b}\left(1 - \dfrac{\tau}{\tau_{\rm cond}}\right), \\ M_{\rm cold} \simeq f_{\rm inf}\,M_{\rm b}\left(\dfrac{\tau}{\tau_{\rm cond}}\right), \\ M_{\star} \simeq \dfrac{s\,f_{\rm inf}\,M_{\rm b}}{2}\left(\dfrac{\tau}{\tau_{\rm cond}}\right)^2, \end{cases} \tag{4}$$

where the dimensionless independent variable x has been reexpressed as $\tau/\tau_{\rm cond}$. In addition, the maximum of the cold gas mass (and SFR) occurs for

$$\tau_{\rm max} = \tau_{\rm cond}\,\ln\left[(s\,\gamma)^{1/(s\,\gamma-1)}\right] \tag{5}$$

when the mass of the various gas components is written

$$\begin{cases} M_{\rm inf}(\tau_{\rm max}) \simeq f_{\rm inf}\,M_{\rm b}\,(s\,\gamma)^{-1/(s\,\gamma-1)}, \\ M_{\rm cold}(\tau_{\rm max}) \simeq f_{\rm inf}\,M_{\rm b}\,(s\,\gamma)^{-s\,\gamma/(s\,\gamma-1)}, \\ M_{\star}(\tau_{\rm max}) \simeq \dfrac{f_{\rm inf}\,M_{\rm b}}{\gamma}[1 - (1 + s\,\gamma)(s\,\gamma)^{-s\,\gamma/(s\,\gamma-1)}]. \end{cases} \tag{6}$$

Finally, for $\tau \gg \tau_{\rm cond}$, the solutions behave as

$$\begin{cases} M_{\rm inf} \simeq f_{\rm inf}\,M_{\rm b}\,e^{-\tau/\tau_{\rm cond}}, \\ M_{\rm cold} \simeq \dfrac{f_{\rm inf}\,M_{\rm b}}{s\,\gamma - 1}\,e^{-\tau/\tau_{\rm cond}}, \\ M_{\star} \simeq \dfrac{f_{\rm inf}\,M_{\rm b}}{\gamma}. \end{cases} \tag{7}$$

These expressions highlight a few interesting facts. First, the overall time behavior of the cold gas mass and SFR

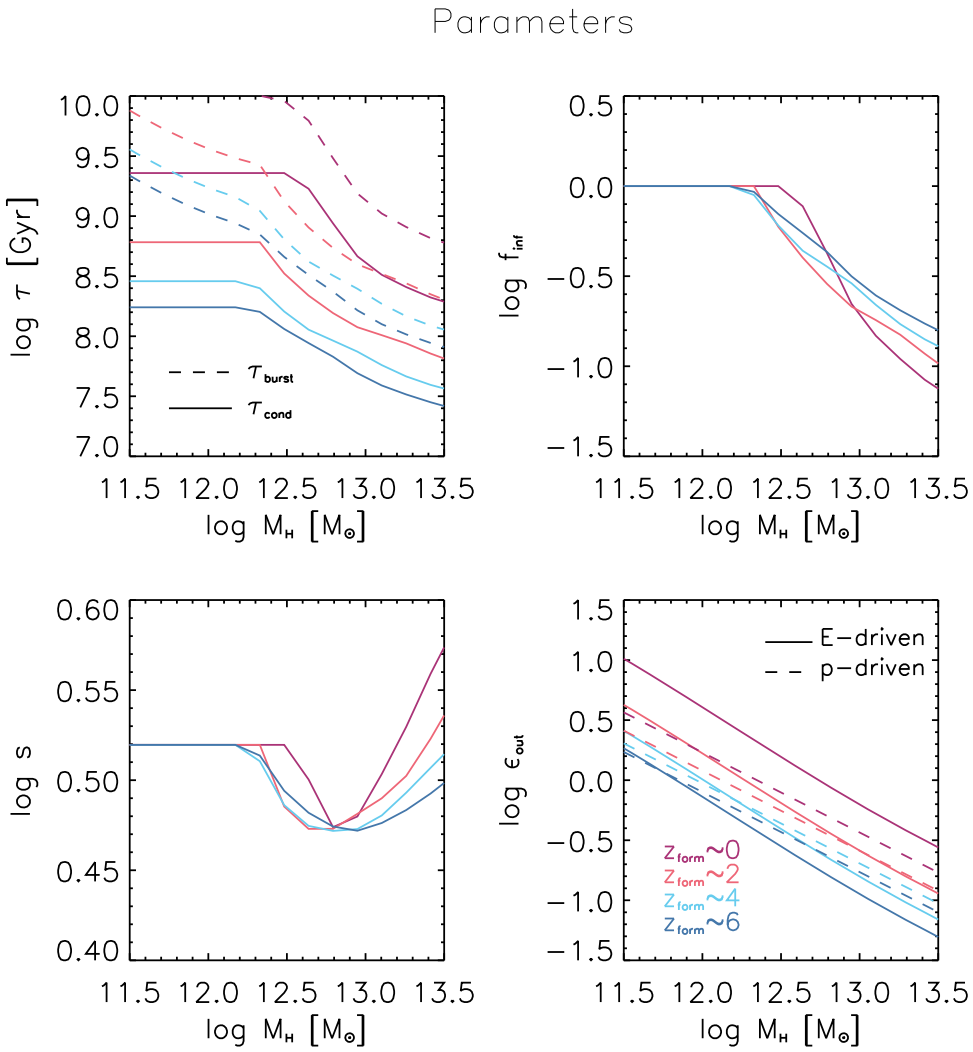

Figure 1. Main parameters entering the analytic solutions relevant for ETG progenitors as a function of host halo mass $M_{\rm H}$ and formation redshift $z_{\rm form}$. Top left panel: condensation timescale $\tau_{\rm cond}$ (solid lines) and duration of the star-forming phase $\tau_{\rm burst}$ (dashed lines). Top right panel: infall fraction $f_{\rm inf}$. Bottom left panel: ratio $s \equiv \tau_{\rm cond}/\tau_\star$ of the star formation to the condensation timescale. Bottom right panel: mass loading factor of the outflows from stellar feedback $\epsilon_{\rm out}$ for energy-driven (solid lines) and momentum-driven (dashed lines) outflows. In all panels, the colors refer to different formation redshifts: $z_{\rm form} = 0$ (red), 2 (orange), 4 (cyan), and 6 (blue).

$\dot{M}_\star(\tau) \propto M_{\rm cold}(\tau)$ is very similar to the empirical delayed exponential shape $\dot{M}_\star \propto \tau^\kappa\, e^{-\tau/\tau_{\rm cond}}$ with $\kappa \lesssim 1$, which is routinely used to describe the star formation histories and interpret the spectral energy distribution (SED) for high-z star-forming galaxies and the progenitors of local spheroids (see Papovich et al. 2011; Moustakas et al. 2013; Steinhardt et al. 2014; da Cunha et al. 2015; Cassará et al. 2016; Citro et al. 2016; Boquien et al. 2019); thus, our solutions may provide a physical basis to that empirical shape. Second, after the peak of the SFR for $\tau \gtrsim \tau_{\rm max}$, the infall rate and SFR are proportional, such that $\dot{M}_{\rm inf} \propto -(s\gamma - 1)\dot{M}_\star$; this explains why models where a similar proportionality is assumed a priori (e.g., Matteucci & Chiosi 1983; Matteucci 2012) produce results not substantially different from those with a generic exponential infall (see Recchi et al. 2008). Third, the specific SFR $({\rm sSFR}) \equiv \dot{M}_\star/M_\star$ is a monotonic function of the galaxy age, since at early times, it behaves like ${\rm sSFR} \simeq 2/\tau$, and at late times, it behaves as ${\rm sSFR} \simeq s\gamma\, e^{-\tau/\tau_{\rm cond}}/(s\gamma - 1)$; thus, a selection in sSFR is equivalent to a selection in galaxy age. Lastly, the true relic stellar mass after the loss due to stellar evolution is

$$M_\star^{\rm relic} \simeq (1 - \mathcal{R})M_\star = \frac{1 - \mathcal{R}}{1 - \mathcal{R} + \epsilon_{\rm out}} f_{\rm inf}\, M_{\rm b}; \qquad (8)$$

thus, in the absence of any outflows $\epsilon_{\rm out} \approx 0$, all of the available (infalling) baryons would be converted into stars.

2.2. Metals

We now turn to discussing the time evolution of the metallicity in cold gas and stellar mass, first focusing on instantaneous production of α-elements by Type II SNe and stellar winds and then turning to the delayed production of iron-group elements by Type Ia SNe.

2.2.1. Cold Gas Metallicity from Instantaneously Produced Elements

The time evolution of the metallicity $Z_{\rm cold}$ in cold gas mass contributed by instantaneously produced chemical elements is

described as

$$\frac{d}{d\tau}(M_{\rm cold}\, Z_{\rm cold}) = -\gamma\, \dot{M}_\star\, Z_{\rm cold} + y_Z(1-\mathcal{R})\, \dot{M}_\star. \quad (9)$$

The equation above prescribes that the mass of metals in cold gas, $M_{\rm cold}\, Z_{\rm cold}$, evolves because of instantaneous metal production at a rate $y_Z\,(1-\mathcal{R})\dot{M}_\star$, outflow depletion at a rate $\epsilon_{\rm out}\, \dot{M}_\star\, Z_{\rm cold}$, and astration (metal mass locking into stellar remnants) at a rate $(1-\mathcal{R})\dot{M}_\star\, Z_{\rm cold}$; we have neglected the infalling gas metallicity that is assumed to be primordial (but can be otherwise included very easily in the analytic solutions). Under the instantaneous mixing and recycling approximation, the metal production yield is given by

$$y_Z \equiv \frac{1}{1-\mathcal{R}} \int_{1\, M_\odot}^{100\, M_\odot} dm_\star m_\star p_{Z,\star}\, \phi(m_\star), \quad (10)$$

where $p_{Z,\star}$ is the mass fraction of newly synthesized metals by the star of initial mass $m_\star$; with this definition relative to $1-\mathcal{R}$, the yield y_Z represents the ratio between the mass of heavy elements ejected by a stellar generation and the mass locked up in remnants.

In many previous analytic models, to solve the chemical evolution equation, an empirical shape of the SFR is adopted; remarkably, here we instead use the self-consistent solutions for the time evolution of the infalling and cold gas masses, recasting Equation (9) into the form

$$\dot{Z}_{\rm cold} = -\frac{Z_{\rm cold}}{\tau_{\rm cond}}\, \frac{s\,\gamma - 1}{1 - e^{-(s\,\gamma-1)\tau/\tau_{\rm cond}}} + \frac{y_Z\,(1-\mathcal{R})s}{\tau_{\rm cond}} \quad (11)$$

with initial condition $Z_{\rm cold}(0) = 0$. The corresponding analytic solution for the cold gas metallicity reads

$$\boxed{Z_{\rm cold}(\tau) = \bar{Z}_{\rm cold}\left[1 - \frac{(s\,\gamma-1)x}{e^{(s\,\gamma-1)x} - 1}\right],} \quad (12)$$

where

$$\bar{Z}_{\rm cold} = \frac{s\, y_Z\,(1-\mathcal{R})}{s\,\gamma - 1} \quad (13)$$

represents the asymptotic value for $\tau \gg \tau_{\rm cond}$. It turns out that the evolution of the gas metallicity is very rapid, so it attains values $\gtrsim Z_\odot/10$ in quite a short timescale $\tau \lesssim \tau_{\rm cond}/10 \approx$ a few 10^7 yr; this will be relevant for the metal and dust enrichment of primordial galaxies and quasars at high redshift (see Section 4.6).

It is instructive to look at the initial behavior of the gas metallicity for $\tau \ll \tau_{\rm cond}$, which reads

$$Z_{\rm cold}(\tau) \simeq \frac{s\, y_Z\,(1-\mathcal{R})}{2}\, \frac{\tau}{\tau_{\rm cond}}; \quad (14)$$

the resulting evolution is thus almost linear with galactic age until a saturation to the final, stationary value $\bar{Z}_{\rm cold}$ takes place. Interestingly, the cold gas metallicity evolution at early times can be expressed in terms of the sSFR $\equiv \dot{M}_\star/M_\star$, such that it behaves like $Z_{\rm cold} \simeq s\, y_Z\,(1-\mathcal{R})/\,{\rm sSFR}\tau_{\rm cond} \propto M_\star/\dot{M}_\star$; thus, a selection based on small $M_\star$ or large sSFR will tend to pick up objects for which the gas metallicity scales inversely with the SFR. On the other hand, at late times, the gas metallicity saturates to a constant value $\bar{Z}_{\rm cold}$; thus, a selection based on large $M_\star$ or small sSFR will tend to pick up galaxies for which the cold gas metallicity is uncorrelated with the SFR. This is the essence of the fundamental metallicity relation, established observationally by Mannucci et al. (2010; see also Lara-Lopez et al. 2013).

Our analytic solution for the gas metallicity is compared with that from classic analytic models in the Appendix.

2.2.2. Cold Gas Metallicity from Delayed Production Elements

We can also deal with a delayed production of metals, related to the iron-group elements, due to Type Ia SNe. To a good approximation, one can decompose $Z_{\rm cold} \simeq Z_{\rm cold}^{\Delta=0} + Z_{\rm cold}^{\Delta}$ into an instantaneous production component $Z_{\rm cold}^{\Delta=0}$, as described in the previous section, and a delayed production component $Z_{\rm cold}^{\Delta}$, governed by the equation

$$\frac{d}{d\tau}(M_{\rm cold}\, Z_{\rm cold}^{\Delta}) = -\gamma\, \dot{M}_\star\, Z_{\rm cold}^{\Delta} + y_Z^{\Delta}(1-\mathcal{R})\, \dot{M}_\star(\tau) \times \frac{\dot{M}_\star(\tau-\Delta)}{\dot{M}_\star(\tau)}, \quad (15)$$

with y_Z^{Δ} the stellar yield for delayed metals, and Δ the delay time for the enrichment by Type Ia SNe that for the moment we consider fixed to some particular value. Notice that this equation is very similar to that for instantaneously produced metals, apart from the factor $\dot{M}_\star(\tau-\Delta)/\dot{M}_\star(\tau)$ in the last term on the right-hand side, which accounts for the delayed contribution of Type Ia SNe in polluting the cold medium.

Using the self-consistent solutions for the SFR, the evolution equation for the delayed metallicity $Z_{\rm cold}^{\Delta}$ is found,

$$\dot{Z}_{\rm cold}^{\Delta} = -\frac{Z_{\rm cold}^{\Delta}}{\tau_{\rm cond}}\, \frac{s\,\gamma - 1}{1 - e^{-(s\,\gamma-1)\tau/\tau_{\rm cond}}} + \frac{y_Z^{\Delta}\,(1-\mathcal{R})s}{\tau_{\rm cond}} \times \frac{e^{\Delta/\tau_{\rm cond}} - e^{s\,\gamma\,\Delta/\tau_{\rm cond}}\, e^{-(s\,\gamma-1)\tau/\tau_{\rm cond}}}{1 - e^{-(s\,\gamma-1)\tau/\tau_{\rm cond}}}, \quad (16)$$

with an initial condition $Z_{\rm cold}^{\Delta}(\tau) = 0$ for $\tau < \Delta$. The corresponding analytic solution reads

$$\boxed{Z_{\rm cold}^{\Delta}(\tau) = \begin{cases} \bar{Z}_{\rm cold}^{\Delta}\left[1 - \dfrac{e^{(s\,\gamma-1)x_\Delta}\,[1 + (s\,\gamma-1)(x-x_\Delta)] - 1}{e^{(s\,\gamma-1)x} - 1}\right] & \text{for } x \geqslant x_\Delta, \\ 0 & \text{for } x < x_\Delta \end{cases}} \quad (17)$$

where $x_\Delta \equiv \Delta/\tau_{\rm cond}$ and $\bar{Z}^{\Delta}_{\rm cold}$ is the delayed metallicity asymptotic behavior for $\tau \gg \tau_{\rm cond}$:

$$\bar{Z}^{\Delta}_{\rm cold} = \frac{s\, y^{\Delta}_Z\, (1-\mathcal{R}) e^{\Delta/\tau_{\rm cond}}}{s\,\gamma - 1}. \tag{18}$$

Note that, as it should be, for $\Delta = 0$, the time dependence in Equation (17) converges to that of cold gas metallicity for instantaneously produced elements in Equation (12). The behavior of $Z^{\Delta}_{\rm cold}$ for $\tau \simeq \Delta$ reads

$$Z^{\Delta}_{\rm cold}(\tau) \simeq \frac{s\, y^{\Delta}_Z (1-\mathcal{R})}{2}\, \frac{(s\gamma-1) e^{s\gamma\,\Delta/\tau_{\rm cond}}}{e^{(s\gamma-1)\Delta/\tau_{\rm cond}} - 1} \left(\frac{\tau-\Delta}{\tau_{\rm cond}}\right)^2. \tag{19}$$

The above solution holds when a single delay time Δ is assumed. However, it is well known that Type Ia SNe feature nontrivial probability DTDs, $dp/d\Delta$. Typically, universal DTDs with shapes $dp/d\Delta \propto \Delta^{-1}$, $\propto e^{-\Delta/\Delta_c}$, $\propto e^{-(\Delta-\bar{\Delta})^2/\sigma^2_\Delta}$, or a combination of these are consistent with observations and widely adopted in chemical evolution models (e.g., Greggio 2005; Mannucci et al. 2006; Totani et al. 2008; Schonrich & Binney 2009; Walcher et al. 2016; Maoz & Graur 2017; for a review and further references, see Maoz et al. 2014). In such a case, one can easily recognize that, since the differential equation involved is linear, the above solution actually constitutes the Green function of the problem, i.e., the solution for a Dirac-$\delta_{\rm D}$ DTD centered at a delay time Δ. Thus, the overall solution for a generic $dp/d\Delta$ is just the superposition of the previous solution for given Δ weighted by the DTD, so that

$$Z^{\rm DTD}_{\rm cold}(\tau) = \int d\Delta\, \frac{dp}{d\Delta}\, Z^{\Delta}_{\rm cold}(\tau). \tag{20}$$

As a working example, we take the analytically convenient exponential DTD with normalized shape $dp/d\Delta = (\omega/\tau_{\rm cond}) e^{-\omega\,\Delta/\tau_{\rm cond}}$, where $\tau_{\rm cond}/\omega$ is the average (typical) DTD timescale. Then one can explicitly compute

$$\boxed{Z^{\rm DTD}_{\rm cold}(\tau) = \bar{Z}^{\rm DTD}_{\rm cold}\left[1 - \left(\frac{s\gamma-1}{s\gamma-\omega}\right)^2 \times \frac{e^{(s\,\gamma-\omega)x} - 1 - x(\omega-1)(s\gamma-\omega)/(s\gamma-1)}{e^{(s\,\gamma-1)x}-1}\right],} \tag{21}$$

where

$$\bar{Z}^{\rm DTD}_{\rm cold} = \frac{s\,\omega\, y^{\Delta}_Z\,(1-\mathcal{R})}{(\omega-1)(s\,\gamma-1)}. \tag{22}$$

As in Equation (3), one can easily check that for $\omega > 0$, the above solution (Equation (21)) is physically meaningful (nonnegative for any x) when $s\gamma > 1$. Note that the solution is also defined for $\omega \simeq 1$ and explicitly writes down as

$$Z^{\rm DTD}_{\rm cold}(\tau) \simeq s\, y^{\Delta}_Z\,(1-\mathcal{R}) \times \left[\frac{x}{s\gamma-1}\,\frac{e^{(s\gamma-1)x}+1}{e^{(s\gamma-1)x}-1} - \frac{2}{(s\gamma-1)^2}\right]. \tag{23}$$

The early-time behavior of Equation (21) for $\tau \ll \tau_{\rm cond}$ reads

$$Z^{\rm DTD}_{\rm cold}(\tau) \simeq \frac{s\,\omega\, y^{\Delta}_Z\,(1-\mathcal{R})}{6}\left(\frac{\tau}{\tau_{\rm cond}}\right)^2, \tag{24}$$

so that initially, the increase in the metallicity of delayed metals $Z^{\rm DTD}_{\rm cold} \propto \tau^2$, even when averaged over the DTD, is clearly retarded with respect to that of instantaneously produced metals $Z_{\rm cold} \propto \tau$. On the other hand, the late-time behavior for $\tau \gg \tau_{\rm cond}$ depends on ω as

$$Z^{\rm DTD}_{\rm cold}(\tau) \simeq \begin{cases} \dfrac{s\,\omega\, y^{\Delta}_Z\,(1-\mathcal{R})}{(\omega-1)(s\,\gamma-1)} & \text{for } \omega > 1, \\ \dfrac{s\, y^{\Delta}_Z\,(1-\mathcal{R})}{s\,\gamma-1}\,\dfrac{\tau}{\tau_{\rm cond}} & \text{for } \omega = 1\ , \\ \dfrac{s\,\omega\, y^{\Delta}_Z\,(1-\mathcal{R})(s\,\gamma-1)}{(1-\omega)(s\,\gamma-\omega)^2}\, e^{(1-\omega)\tau/\tau_{\rm cond}} & \text{for } \omega < 1 \end{cases}$$

so that the solution converges for $\omega > 1$ to $\bar{Z}^{\rm DTD}_{\rm cold}$, while it diverges linearly for $\omega = 1$ and exponentially for $\omega < 1$; however, these divergences occur only at very late times, so the solution behaves very similarly out to $\tau/\tau_{\rm cond} \lesssim 10^2$ for any value of ω.

2.2.3. Stellar Metallicity

The metallicity $Z_\star$ in the stellar component is computed by averaging the cold gas metallicity over the star formation history,

$$Z_\star(\tau) = \frac{1}{M_\star(\tau)} \int_0^\tau d\tau' Z_{\rm cold}(\tau')\dot{M}_\star(\tau'), \tag{25}$$

so that $Z_\star$ represents the amount of metal stocked in the stellar component. Using the self-consistent expression of the cold gas metallicity for instantaneously produced elements, one obtains

$$\boxed{Z_\star(\tau) = \bar{Z}_\star\left[1 - \frac{s\,\gamma}{s\,\gamma-1}\,\frac{e^{-x} - e^{-s\,\gamma\,x}\,[1+(s\,\gamma-1)x]}{s\gamma - 1 + e^{-s\,\gamma\,x} - s\gamma\, e^{-x}}\right],} \tag{26}$$

where the asymptotic behavior for $\tau \gg \tau_{\rm cond}$ writes as

$$\bar{Z}_\star = \frac{y_Z(1-\mathcal{R})}{\gamma} = \frac{s\gamma-1}{s\gamma}\,\bar{Z}_{\rm cold}; \tag{27}$$

it is seen that our analytic solutions, differently from other models in the literature, predict that the stellar metallicity is not equal but rather somewhat lower than the cold gas one. The early-time behavior of $Z_\star$ for $\tau \ll \tau_{\rm cond}$ reads

$$Z_\star(\tau) \simeq \frac{s\, y_Z\,(1-\mathcal{R})}{3}\,\frac{\tau}{\tau_{\rm cond}}, \tag{28}$$

so that initially, $Z_\star(\tau) \simeq 2\, Z_{\rm cold}(\tau)/3$; i.e., the stellar and cold gas metallicity evolve in parallel.

An analogous computation can be performed for the delayed cold gas metallicity (see Section 2.2.2) by inserting $Z^{\Delta}_{\rm cold}$ from Equation (17) into Equation (25) to yield

$$Z_\star^\Delta(\tau) = \begin{cases} \bar{Z}_\star^\Delta \left[1 - \dfrac{s\,\gamma}{s\,\gamma - 1}\,\dfrac{e^{-(x-x_\Delta)} - e^{-s\,\gamma\,(x-x_\Delta)}\,[1 + (s\,\gamma - 1)(x - x_\Delta)]}{s\gamma - 1 + e^{-s\,\gamma\,x} - s\gamma\,e^{-x}} + \right. \\ \left. - \dfrac{e^{-s\gamma\,x} - e^{-s\,\gamma(x-x_\Delta)} - s\gamma\,[e^{-x} - e^{-(x-x_\Delta)}]}{s\gamma - 1 + e^{-s\,\gamma\,x} - s\gamma\,e^{-x}}\right], & \text{for } x \geqslant x_\Delta \\ 0 & \text{for } x < x_\Delta \end{cases}, \tag{29}$$

where the value for $\tau \gg \tau_{\rm cond}$ reads

$$\bar{Z}_\star^\Delta = \frac{y_Z^\Delta (1 - \mathcal{R})}{\gamma}. \tag{30}$$

It is interesting to note that, if star formation proceeded for long times, the ratio of the stellar metallicity for instantaneously and delayed elements would amount to $\bar{Z}_\star^{\Delta=0}/\bar{Z}_\star^\Delta \approx y_Z/y_Z^\Delta$, i.e., the ratio of the respective yields. On the contrary, if star formation is quenched after some time (as is the case for massive galaxies because of BH feedback; see Section 3.2), then the different evolution of $Z_\star^{\Delta=0}$ in Equation (26) and $Z_\star^\Delta$ in Equation (29) would imply an underabundance of delayed with respect to instantaneously produced elements; this will be at the origin of the α-enhancement (see Section 4.7).

Note that, as it should be, for $\Delta = 0$, the time dependence in Equation (29) converges to that of the stellar metallicity for instantaneously produced elements in Equation (26). The behavior of $Z_\star^\Delta$ for $\tau \simeq \Delta$ reads

$$Z_\star^\Delta(\tau) \simeq \frac{s\,y_Z^\Delta\,(1 - \mathcal{R})}{6} \times \frac{s\gamma(s\gamma - 1)}{s\gamma - 1 + e^{-s\gamma\,x_\Delta} - s\gamma\,e^{-x_\Delta}} \left(\frac{\tau - \Delta}{\tau_{\rm cond}}\right)^3. \tag{31}$$

In case of a nontrivial SN Type Ia DTD, $dp/d\Delta$, the overall solution for the stellar metallicity may be derived from

$$Z_\star^{\rm DTD}(\tau) = \int d\Delta\,\frac{dp}{d\Delta}\,Z_\star^\Delta(\tau) = \frac{1}{M_\star(\tau)} \times \int_0^\tau d\tau' Z_{\rm cold}^{\rm DTD}(\tau')\dot{M}_\star(\tau'); \tag{32}$$

the expression for an exponential DTD is still analytic but rather cumbersome, so we do not report it here.

2.3. Dust

We now turn to describing in simple analytic terms the global evolution of the dust mass and dust-to-gas mass ratio. As in many previous analytic approaches, we assume that dust consists of two interlinked components, namely, a refractory *core* and a volatile *mantle*, subject to the evolution equations

$$\begin{cases} \dfrac{d}{d\tau}(M_{\rm cold}\,D_{\rm core}) = -\gamma\,\dot{M}_\star\,D_{\rm core} - \kappa_{\rm SN}\,\dot{M}_\star\,D_{\rm core} + y_D(1 - \mathcal{R})\dot{M}_\star, \\ \dfrac{d}{d\tau}(M_{\rm cold}\,D_{\rm mantle}) = -\gamma\,\dot{M}_\star\,D_{\rm mantle} - \kappa_{\rm SN}\,\dot{M}_\star\,D_{\rm mantle} + \epsilon_{\rm acc}\,\dot{M}_\star\,D_{\rm core}(Z - D_{\rm mantle}). \end{cases} \tag{33}$$

The first equation prescribes that the evolution of the mass in grain cores $M_{\rm cold}\,D_{\rm core}$ results from the competition of various processes: production due to stellar evolution at a rate $y_D(1 - \mathcal{R})\dot{M}_\star$ with an average yield $y_{\rm D}$; astration by star formation and ejection from galactic outflows that combine in the rate term $-\gamma\,\dot{M}_\star\,D_{\rm core}$; and dust sputtering, spallation, and destruction via SN shock waves at a rate $\kappa_{\rm SN}\,\dot{M}_\star\,D_{\rm core}$ with a strength parameter $\kappa_{\rm SN}$. The second equation describes the evolution of the mass in the dust mantles, which differs from the previous one for the production term: mantle growth is assumed to be driven by accretion of metals onto preexisting grain cores at a rate $\epsilon_{\rm acc}\,\dot{M}_\star\,D_{\rm core}\,(Z - D_{\rm mantle})$ with an efficiency $\epsilon_{\rm acc}$.

Using the self-consistent expression for the cold gas mass, Equation (33) can be recast in terms of the dust mass fractions

$$\begin{cases} \dot{D}_{\rm core} = -\dfrac{D_{\rm core}}{\tau_{\rm cond}}\left[s\,\kappa_{\rm SN} + \dfrac{s\,\gamma - 1}{1 - e^{-(s\,\gamma - 1)x}}\right] + \dfrac{y_D\,(1 - \mathcal{R})s}{\tau_{\rm cond}}; \\ \dot{D}_{\rm mantle} = -\dfrac{D_{\rm mantle}}{\tau_{\rm cond}}\left[s\,\kappa_{\rm SN} + s\,\epsilon_{\rm acc}\,D_{\rm core} + \dfrac{s\,\gamma - 1}{1 - e^{-(s\,\gamma - 1)x}}\right] + \dfrac{s\,\epsilon_{\rm acc}\,D_{\rm core}}{\tau_{\rm cond}}\,Z_{\rm cold}, \end{cases} \tag{34}$$

with initial conditions $D_{\rm core}(0) = D_{\rm mantle}(0) = 0$. The corresponding analytic solution for grain cores is

$$\boxed{D_{\rm core}(\tau) = \bar{D}_{\rm core}\left[1 - \frac{s\,\gamma - 1}{e^{(s\,\gamma - 1)x} - 1}\,\frac{1 - e^{-s\,\kappa_{\rm SN}\,x}}{s\,\kappa_{\rm SN}}\right]}, \tag{35}$$

where the asymptotic value for $\tau \gg \tau_{\rm cond}$ reads

$$\bar{D}_{\rm core} = \frac{s\,y_D\,(1 - \mathcal{R})}{s(\gamma + \kappa_{\rm SN}) - 1}. \tag{36}$$

In solving the equation for the mantle, we assume the core fraction $D_{\rm core}(\tau)$ to be fixed at its asymptotic value $\bar{D}_{\rm core} \ll \bar{Z}_{\rm cold}$, since from Equation (35), this is seen to be attained very rapidly after a time $\tau \gtrsim \tau_{\rm cond}/s\,\kappa_{\rm SN}$ for typical values of the parameters (see Section 3.3 this amounts to a few $10^{-2}\,\tau_{\rm cond}$). We then obtain

$$D_{\rm mantle}(\tau) = \bar{D}_{\rm mantle}\left\{1 - \frac{(s\,\gamma - 1)x}{e^{(s\,\gamma-1)x} - 1} \times \left[1 + \frac{s\,\gamma - 1}{s\,\tilde{\epsilon}}\left(1 - \frac{1 - e^{-s\,\tilde{\epsilon}\,x}}{s\,\tilde{\epsilon}\,x}\right)\right]\right\}, \quad (37)$$

where $\tilde{\epsilon} \equiv \kappa_{\rm SN} + \epsilon_{\rm acc}\,\bar{D}_{\rm core}$ and the asymptotic value for $\tau \gg \tau_{\rm cond}$ reads

$$\bar{D}_{\rm mantle} = \frac{s\,\epsilon_{\rm acc}\,\bar{D}_{\rm core}\,\bar{Z}_{\rm cold}}{s(\gamma + \kappa_{\rm SN} + \epsilon_{\rm acc}\,\bar{D}_{\rm core}) - 1}; \quad (38)$$

thus, if the accretion process is very efficient, Equation (38) implies that the final dust fraction tends to the gas metallicity. The early-time behavior for $\tau \ll \tau_{\rm cond}$ writes as

$$\begin{cases} D_{\rm core}(\tau) \simeq \dfrac{s\,y_D(1-\mathcal{R})}{2}\,\dfrac{\tau}{\tau_{\rm cond}}, \\ D_{\rm mantle}(\tau) \simeq \dfrac{s^3}{6}\,\dfrac{\epsilon_{\rm acc}\,y_D\,y_Z(1-\mathcal{R})^2}{s\,(\gamma + \kappa_{\rm SN}) - 1}\left(\dfrac{\tau}{\tau_{\rm cond}}\right)^2, \end{cases} \quad (39)$$

so that the mantle component overwhelms the core one soon after dust production has started. Note that the second equation above is strictly valid for times $\tau_{\rm cond}/s\kappa_{\rm SN} \lesssim \tau \lesssim \tau_{\rm cond}$, when $D_{\rm core}$ has already saturated to its asymptotic value $\bar{D}_{\rm core}$.

It is worth stressing that total dust production and enrichment (core plus mantle) are in general very rapid with respect to the condensation timescale, of order a few $10^{-1}\,\tau_{\rm cond}$; this will be extremely relevant for very high redshift star-forming galaxies and quasar hosts (see Section 4.5).

2.4. Outflowing Mass and Metals

The effect of galactic outflows driven by SN explosions and stellar winds is to heat and remove the cold gas at a rate $\epsilon_{\rm out}\,\dot{M}_\star$ proportional to the SFR. One can also include a sort of impulsive energy/momentum feedback; e.g., this may be driven by emission from the central supermassive BH that in the progenitors of elliptical galaxies is thought to quench star formation. To a crude approximation, the action of such impulsive feedback can be described as heating/ejection of all the residual mass in cold gas $M_{\rm cold}(\tau_{\rm burst})$ at a galactic age $\tau_{\rm burst}$. Then the overall outflowing gas mass at $\tau_{\rm burst}$ reads

$$M_{\rm out} = \epsilon_{\rm out}\,M_\star(\tau_{\rm burst}) + M_{\rm cold}(\tau_{\rm burst}). \quad (40)$$

In addition, the metallicity of the mass outflow by SNe and stellar winds is $\epsilon_{\rm out}\,Z_\star$, while the one associated with impulsive feedback is $Z_{\rm cold}(\tau_{\rm burst})$. Thus, the average metallicity of the outflowing gas at $\tau_{\rm burst}$ writes as

$$Z_{\rm out} = \frac{\epsilon_{\rm out}\,Z_\star(\tau_{\rm burst})M_\star(\tau_{\rm burst}) + Z_{\rm cold}(\tau_{\rm burst})M_{\rm cold}(\tau_{\rm burst})}{\epsilon_{\rm out}\,M_\star(\tau_{\rm burst}) + M_{\rm cold}(\tau_{\rm burst})} \quad (41)$$

and is found to strike an intermediate course between the cold gas and the stellar metallicity. This will be relevant for the enrichment of the warm and hot medium pervading/surrounding massive ETGs (see Section 4.8).

3. Application to ETGs and Their Star-forming Progenitors

We now specialize the analytic solutions presented in the previous sections to a particular issue: the formation of ETGs and the evolution of their high-z star-forming progenitors. To this purpose, in Sections 3.1–3.3, we set the parameters entering our analytic solutions via physical arguments inspired by in situ galaxy-BH coevolution scenarios for ETG formation (e.g., Granato et al. 2004; Lapi et al. 2006, 2014, 2018), with a particular focus on the role of cooling/condensation and feedback processes. Then, in Section 3.4 we discuss the mass additions by mergers in the DM and stellar components, and in Section 3.5 we describe how to deal with different formation redshifts in order to obtain observable spatially averaged quantities.

3.1. Infall Fraction and Star Formation Timescales

To start with, we set the infall fraction $f_{\rm inf}$, condensation timescale $\tau_{\rm cond}$, and ratio of star formation to condensation timescale $s = \tau_{\rm cond}/\tau_\star$ entering the analytic solutions (in particular, the boxed equations in Section 2). Based on the in situ galaxy-BH coevolution scenario by Lapi et al. (2018), we recall here the basic notions relevant for the present context and refer the reader to that paper for an extended discussion.

The in situ scenario envisages that only a fraction $f_{\rm inf} = M_{\rm inf}/f_b\,M_{\rm H}$ of the available baryons $f_b\,M_{\rm H}$ in a halo of mass $M_{\rm H}$, initially located within a radius $R_{\rm inf}$, is able to cool and fall in toward the central region of the galaxy where strong star formation takes place. The radius $R_{\rm inf}$ and the infall fraction can be estimated along the following lines. Given a halo of mass $M_{\rm H}$ formed at redshift $z_{\rm form}$, its virial radius and circular velocity are approximately given by $R_{\rm H} \approx 110\,M_{\rm H,12}^{1/3}\,[E_{z_{\rm form}}/E_{z_{\rm form}=2}]^{-1/3}$ kpc and $v_{c,\rm H} \approx 200\,M_{\rm H,12}\,[E_{z_{\rm form}}/E_{z_{\rm form}=2}]^{1/6}$ km s^{-1} in terms of the redshift-dependent factor $E_{z_{\rm form}} = \Omega_\Lambda + \Omega_M(1+z_{\rm form})^3$ and the normalized halo mass $M_{\rm H,12} = M_{\rm H}/10^{12}\,M_\odot$. Adopting a standard Navarro–Frenk–White (NFW; Navarro et al. 1997) profile for the DM component yields an approximate scaling[6] $M_{\rm H}(<r) \propto r$, so that $R_{\rm inf} \simeq f_{\rm inf}\,R_{\rm H}$ and $M_{\rm H}(<R_{\rm inf}) \simeq f_{\rm inf}\,M_{\rm H}(<R_{\rm H})$; therefore, the dynamical time at $R_{\rm inf}$ is given by

$$t_{\rm dyn}(R_{\rm inf}) \simeq \frac{\pi}{2}\sqrt{\frac{R_{\rm inf}^3}{G\,M_{\rm H}(<R_{\rm inf})}} \approx 6\times10^8\,f_{\rm inf} \times [E_{z_{\rm form}}/E_{z_{\rm form}=2}]^{-1/2}\ {\rm yr}. \quad (42)$$

On the other hand, the cooling time at $R_{\rm inf}$ reads

$$t_{\rm cool}(R_{\rm inf}) \simeq \frac{3\,k_{\rm B}T}{2\,\mu\,\mathcal{C}\,n(R_{\rm inf})\Lambda(T,Z)}, \quad (43)$$

where T is the temperature, $\mu \approx 0.6$ is the mean molecular weight, $n(R_{\rm inf})$ is the gas density, $\mathcal{C}$ is the clumping factor, and $\Lambda(T, Z)$ is

[6] For an NFW profile, the logarithmic slope of the mass distribution $M_{\rm H}(<r) \propto r^\mu$ reads $\mu \equiv d\log M_{\rm H}/d\log r = [c\,x/(1+c\,x)]^2\,[\ln(1+c\,x) - c\,x(1+c\,x)]^{-1}$ in terms of the normalized radius $x \equiv r/R_{\rm H}$ and the concentration parameter c. For a concentration $c \approx 4$ typical of massive galaxy halos formed at $z_{\rm form} \approx 2$ (e.g., Bullock et al. 2001; Zhao et al. 2003), the slope μ takes on values from 0.8 to 1.2 in moving from $R_{\rm H}$ to 0.3 $R_{\rm H}$ and can be effectively approximated with unity down to ∼0.4–0.6 $R_{\rm H}$. For smaller radii, the slope progressively approaches the central value $\mu \sim 2$, which can be approximately used for $r \lesssim 0.1\,R_{\rm H}$.

the cooling function in cgs units dependent on temperature and metallicity (e.g., Sutherland & Dopita 1993). The infalling gas is expected to have temperatures close to the virial $T \simeq 0.5\,\mu m_p\,v_{c,\rm H}^2 \approx 1.5\times10^6\,M_{\rm H,12}^{2/3}\,[E_{z_{\rm form}}/E_{z_{\rm form}=2}]^{1/3}$ K; correspondingly, $\Lambda(T,\ Z) \gtrsim 2\times10^{-23}$ erg cm^3 s^{-1} for $Z \gtrsim Z_\odot/10$ (recall from Section 2.2 that this value is attained quite rapidly within $\lesssim 10^{-1}\,\tau_{\rm cond} \sim$ a few 10^7 yr). The gas density is expected to be on the order of the average baryon density within $R_{\rm inf}$, which reads $n(R_{\rm inf}) \approx 4\times10^{-4}\,f_{\rm inf}^{-2}\,[E_{z_{\rm form}}/E_{z_{\rm form}=2}]$ cm^{-3} having assumed $n(r)$ to follow an isothermal distribution; the clumping factor is expected to be close to that in the intergalactic medium, which cosmological simulations (see Iliev et al. 2007; Pawlik et al. 2009; Finlator et al. 2012; Shull et al. 2012) indicate around $\mathcal{C} \sim$ 6–20 at $z \simeq 2$, so we take $\mathcal{C} \approx 10$.

When $t_{\rm dyn} \lesssim t_{\rm cool}$, the gas can cool efficiently and infall toward the central regions on the dynamical timescale; therefore, we set $f_{\rm inf}$ by requiring that the above dynamical $t_{\rm dyn}(R_{\rm inf}) \propto f_{\rm inf}$ and cooling time $t_{\rm cool} \propto f_{\rm inf}^2$ match. Then we prescribe that the fraction $f_{\rm inf}$ of the baryons located within $R_{\rm inf}$ can cool and condense toward the central regions over a timescale $\tau_{\rm cond} \approx t_{\rm dyn}(R_{\rm inf})$. We plot $f_{\rm inf}$ and $\tau_{\rm cond}$ as a function of the halo mass and formation redshift in Figure 1. The parameter $f_{\rm inf}$ is essentially unity for halo masses $M_{\rm H} \lesssim$ a few $10^{12}\,M_\odot$, while for larger masses, it drops to low values because cooling becomes progressively inefficient and prevents condensation toward the central regions; the dependence on formation redshift is negligible. As to $\tau_{\rm cond}$, it scales with halo mass similarly to $f_{\rm inf}$, while the constant value for $M_{\rm H} \lesssim$ a few $10^{12}\,M_\odot$ depends on formation redshift approximately as $(1+z_{\rm form})^{-3/2}$, reflecting the increased density of the ambient medium at earlier cosmic epochs.

To proceed further, note that such infalling gas rotates, being endowed with the specific angular momentum

$$j_{\rm inf} \equiv f_{\rm inf}\,j_{\rm H} \approx 1100\,f_{\rm inf}\,\lambda_{0.035}\,M_{\rm H,12}^{2/3} \times [E_{z_{\rm form}}/E_{z_{\rm form}=2}]^{-1/6}\ {\rm km\ s^{-1}\ kpc}; \quad (44)$$

here $j_{\rm H} \equiv \sqrt{2}\,\lambda\,R_{\rm H}\,v_{c,\rm H}$ is the halo specific angular momentum and $\lambda_{0.035} \equiv \lambda/0.035$ is the halo spin parameter. Numerical simulations (see Barnes & Efstathiou 1987; Bullock et al. 2001; Macció et al. 2007; Zjupa & Springel 2017) have shown that λ exhibits a lognormal distribution with average value $\langle\lambda\rangle \approx 0.035$ and dispersion $\sigma_{\log\lambda} \approx 0.25$ dex, nearly independent of mass and redshift. In deriving the above equation, the specific angular momentum of the baryonic gas has been assumed to initially follow the radial profile of the DM's $j_{\rm H}(<r) \propto M_{\rm H}^{\alpha}(<r)$ with $\alpha \approx 1$, which in turn is found from simulations to closely follow the mass profile (e.g., Bullock et al. 2001; Shi et al. 2017).

Given that $j_{\rm inf}$ is approximately conserved, the inflow of the gas from $R_{\rm inf}$ toward the central region can proceed until the radius $R_{\rm rot}$, where the rotational support balances the gravitational pull, i.e., $G\,M_{\rm tot}(<R_{\rm rot})/R_{\rm rot}^2 = j_{\rm inf}^2/R_{\rm rot}^3$; such a condition yields

$$R_{\rm rot} \simeq \frac{j_{\rm inf}^2}{G\,M_{\rm inf}} \approx 1.5\,\lambda_{0.035}^2 f_{\rm inf}\,[E_{z_{\rm form}}/E_{z_{\rm form}=2}]^{-1/3}\ {\rm kpc}, \quad (45)$$

and the corresponding dynamical time amounts to

$$t_{\rm dyn}(R_{\rm rot}) \simeq \frac{\pi}{2}\sqrt{\frac{R_{\rm rot}^3}{G\,M_{\rm inf}}} \approx 4\times10^6\,\lambda_{0.035}^3 f_{\rm inf} \times [E_{z_{\rm form}}/E_{z_{\rm form}=2}]^{-1/2}\ {\rm yr}. \quad (46)$$

Recent observations of high-redshift star-forming galaxies have revealed that most of the SFR occurs within a compact region a few kpc under heavy enshrouded conditions (e.g., Scoville et al. 2014, 2016; Ikarashi et al. 2015; Simpson et al. 2015; Straatman et al. 2015; Spilker et al. 2016; Tadaki et al. 2017a, 2017b); in particular, the size $R_{\rm rot}$ derived above has been shown by Lapi et al. (2018) to be consistent with those measured via far-IR/submillimeter and CO line observations of $z \sim$ 1–2 star-forming galaxies (e.g., Barro et al. 2016, 2017; Hodge et al. 2016; Tadaki et al. 2017a; Talia et al. 2018; Lang et al. 2019). Further infall of the gas within $R_{\rm rot}$ can only occur by spreading out specific angular momentum via dynamical friction and gravitational torques, as indicated by specific simulations and suggested by dynamical measurements in high-redshift star-forming galaxies (see Dekel et al. 2009; Genzel et al. 2011; Zolotov et al. 2015; for a review, see Bournaud 2016 and references therein); eventually, these processes will cause a significant smearing of the initial correlation between the baryon and halo specific angular momenta, especially in the high-redshift progenitors of ETGs, where angular momentum loss is expected to drive formation of a substantial bulge component (e.g., Danovich et al. 2015; Jiang et al. 2019).

The cold baryonic gas mass $M_{\rm cold}(R_{\rm rot}) \lesssim f_{\rm inf}\,f_b\,M_{\rm H} \sim 10^{10}$–$10^{11}\,M_\odot$, namely, a fraction $f_{\rm inf}$ of the baryons already present in the halo at formation, will be driven by such processes within $R_{\rm rot} \sim$ kpc and form stars on a timescale $t_{\rm SFR}(R_{\rm rot}) \approx 50\times t_{\rm dyn}(R_{\rm rot}) \approx$ (1–2) $\times\,10^8$ yr (see Elmegreen et al. 2005; Krumholz et al. 2012 and references therein), implying SFRs $\dot{M}_\star \lesssim M_{\rm cold}(R_{\rm rot})/t_{\rm SFR} \lesssim 10^2$–$10^3\,M_\odot$ yr^{-1} and hence rapid metallicity enrichment and dust formation. These conditions have indeed been observed in ETG progenitors, in particular via high-resolution interferometric observations with ALMA (see Scoville et al. 2016; Barro et al. 2017; Tadaki et al. 2017a, 2017b; Talia et al. 2018; Lang et al. 2019). Note that in such systems, cooling and the ensuing star formation from baryons accreted during later halo growth over cosmological timescales will be hampered by the effects of stellar and active galactic nucleus (AGN) feedback (see below); this is at variance with respect to present-day disk-dominated galaxies, where the cold gas accretion is not inhibited by strong feedback and the star formation process is prolonged over several Gyr. On the basis of the above discussion, we set the parameter $s \equiv \tau_{\rm cond}/\tau_\star$ entering our analytic solutions as $s = t_{\rm dyn}(R_{\rm inf})/t_{\rm SFR}(R_{\rm rot})$; in Figure 1, it is shown to take on values around 3–3.5, weakly dependent on halo mass and formation redshift.

3.2. Feedback Parameters

Another important parameter entering our analytic solutions is the mass loading factor $\epsilon_{\rm out}$ of slow outflows related to Type II SNe and stellar winds. We adopt the standard expression used in many literature studies since the pioneering work of White & Frenk (1991; for reviews and further references, see

Mo et al. 2010 and Somerville & Dave 2015),

$$\epsilon_{\rm out} = \frac{\epsilon_{\rm SN}\,\eta_{\rm SN}\,E_{\rm SN}}{E_{\rm bind}} \approx \epsilon_{\rm SN,0.05}\,\eta_{\rm SN,-2}\,E_{\rm SN,51}\,M_{\rm H,12}^{-2/3} \times [E_{z_{\rm form}}/E_{z_{\rm form}=2}]^{-1/3}, \quad (47)$$

in terms of the occurrence $\eta_{\rm SN,-2} = \eta_{\rm SN}/0.01\,M_\odot$ of SNe per unit solar mass formed into stars (apt for our fiducial Chabrier IMF), the average energy $E_{\rm SN,51} = E_{\rm SN}/10^{51}$ erg per single SN explosion, the energy fraction $\epsilon_{\rm SN,0.05} = \epsilon_{\rm SN}/0.05$ effectively coupled to the interstellar medium and available to drive the outflow (comparable to the overall coupled energy when cooperative SN blast-wave propagation takes place, like in violent starbursts; e.g., Mac Low & Ferrara 1999; Mo et al. 2010), and the gas specific binding energy $E_{\rm bind} \approx 2.5 \times 10^{14}\,M_{\rm H,12}^{2/3}\,[E_{z_{\rm form}}/E_{z_{\rm form}=2}]^{1/3}\,{\rm cm^2\,s^{-2}}$ in the halo potential well (see Zhao et al. 2003; Mo & Mao 2004). The outcome is illustrated in Figure 1 as a function of halo mass and formation redshift; it takes on values in the range $\epsilon_{\rm out} \sim 0.1$–10 for halo masses $M_{\rm H} \sim 10^{13.5}$–$10^{11}\,M_\odot$, with a weak dependence on formation redshift. Such a behavior is indeed in agreement with self-consistent hydrodynamical simulations of stellar feedback (e.g., Hopkins et al. 2012).

Note that Equation (47) is meant to describe an energy-driven slow outflow that can offset gas infall from large scales out to $R_{\rm inf} \gg R_{\rm rot}$, where the binding energy is dominated by the dark matter halo. An alternative prescription for stellar feedback invokes momentum-driven outflows (e.g., Murray et al. 2005; Oppenheimer & Dave 2006) that, in our context, can indeed operate to blow some of the cold gas out of $R_{\rm rot}$, where the binding energy is largely dominated by baryons; in such a case, the relevant mass loading factor reads $\epsilon_{\rm out} = \eta_{\rm SN}\,E_{\rm SN}/v_{\rm SN}\,v_{\rm rot} \approx v_{\rm SN,3}\,\eta_{\rm SN,-2}\,E_{\rm SN,51}\,\lambda_{0.035}\,M_{\rm H,12}^{-2/3}\,[E_{z_{\rm form}}/E_{z_{\rm form}=2}]^{-1/6}$ in terms of the typical velocity of SN ejecta $v_{\rm SN,3} \equiv v_{\rm SN}/10^3\,{\rm km\ s^{-1}}$ and the escape velocity $v_{\rm rot} \approx j_{\rm inf}/R_{\rm rot}$ at $R_{\rm rot}$. The resulting $\epsilon_{\rm out}$ for the energy- and momentum-driven outflows is comparable within the uncertainties of the parameters entering the respective expressions (see Figure 1) and produces similar evolution in the gas/stellar mass and metallicity when used in our analytic solutions.

Another form of feedback that is thought to be extremely relevant in the formation of ETGs is related to the hosted accreting supermassive BH (see, e.g., Silk & Rees 1998; Fabian 1999; King 2003; Granato et al. 2004; Murray et al. 2005; Lapi et al. 2006, 2014; for a review, see King 2014 and references therein). In this paper, we do not aim at building up a self-consistent model of the coevolution between a star-forming galaxy and the central supermassive BH, but we will describe phenomenologically the impact of BH feedback on the host galaxy by abruptly quenching the star formation and ejecting the residual gas mass after a time $\tau_{\rm burst}$. Constraints on $\tau_{\rm burst}$ come from SED modeling of dusty ETG star-forming progenitors (see Papovich et al. 2011; Moustakas et al. 2013; Steinhardt et al. 2014; da Cunha et al. 2015; Cassará et al. 2016; Citro et al. 2016; Boquien et al. 2019) that suggest a duration of $\lesssim$0.5–1 Gyr for massive galaxies with $M_\star \gtrsim$ a few $10^{10}\,M_\odot$. Similar values in massive ETGs are also concurrently indicated by local observations of the stellar mass–metallicity relationship and of the α-enhancement, i.e., iron under-abundance compared to α-elements (occurring because star formation is stopped before Type Ia SN explosions can pollute the interstellar medium with substantial amounts of iron; e.g., Thomas et al. 2005; Gallazzi et al. 2006, 2014; for a review, see Renzini 2006). On the contrary, in low-mass spheroidal galaxies with $M_\star \lesssim 10^{10}\,M_\odot$, data on the age of the stellar population and chemical abundances indicate that star formation proceeded for longer times, mainly regulated by SN feedback and stellar winds (see review by Conroy 2013). On this basis, we phenomenologically parameterize the timescale for the duration of the main SFR episode via the smooth expression

$$\tau_{\rm burst} \simeq 3\,\tau_{\rm cond}(1 + M_{\rm H,12}^{-1}), \quad (48)$$

holding in the range $M_{\rm H} \sim 10^{11}$–$10^{13.5}\,M_\odot$. This formula is meant to interpolate between the aforementioned behaviors for less and more massive galaxies; e.g., at $z_{\rm form} \approx 2$, it prescribes short timescales $\tau_{\rm burst} \sim$ a few 10^8 yr for galaxies in massive halos with $M_{\rm H} \sim 10^{13}\,M_\odot$ and appreciably longer $\tau_{\rm burst} \sim$ several 10^9 for galaxies in small halos with $M_{\rm H} \sim 10^{11.5}\,M_\odot$. We have checked that our results are rather insensitive to the specific shape of such a phenomenological parameterization. With a similar formula, Mancuso et al. (2016a, 2016b) reproduced the MS of star-forming galaxies at $z \approx 2$, and Lapi et al. (2017) linked the statistics of star-forming galaxies, AGNs, and massive quiescent galaxies via a continuity equation approach.

Thus, infall, condensation, and feedback processes actually set the main parameters entering our analytic solutions.

3.3. Yields and Other IMF-related Parameters

Other relevant parameters are mainly determined by the adopted Chabrier (2003, 2005) IMF and the Romano et al. (2010) stellar yield models. We compute an instantaneous recycling fraction $\mathcal{R} \approx 0.45$, an average yield of instantaneously produced metals $y_Z \approx 0.06$, and a yield of oxygen $y_O \approx 0.04$ (see also Krumholz et al. 2012; Feldmann 2015; Vincenzo et al. 2016). Note that these values are weakly dependent on the chemical composition and somewhat dependent on the stellar yield models (e.g., Romano et al. 2010; Nomoto et al. 2013; Vincenzo et al. 2016); e.g., the metal yield can vary within the range $y_Z \sim 0.05$–0.07.

The yield for delayed metals is adopted to be $y_Z^\Delta \approx 2.7 \times 10^{-3}$. This has been computed by taking into account that the occurrence of Type Ia SNe is around $2 \times 10^{-3}\,M_\odot$ per stellar mass formed, and that $0.63\,M_\odot$ of iron-group elements are produced, on average, per explosion (see Bell et al. 2003; Maoz et al. 2014). The outcome is also consistent with the normalization of the observed Type Ia SN DTD (e.g., Vincenzo et al. 2017).

Finally, in the treatment of dust production, we adopt a dust yield $y_{\rm D} \approx 7 \times 10^{-4}$ (see Bianchi & Schneider 2007; Zhukovska et al. 2008; Feldmann 2015), a strength parameter $\kappa_{\rm SN} \approx 10$ for dust spallation by SN winds (see McKee 1989; de Bennassuti et al. 2014), and an efficiency for dust accretion $\epsilon_{\rm acc} \approx 10^5$ (see Hirashita 2000; Asano et al. 2013; Feldmann 2015). These parameters are rather uncertain and mainly set based on previous literature and obtaining a good match to the dust–versus–stellar mass relationship observed in $z \gtrsim 2$ star-forming galaxies.

3.4. Halo and Stellar Mass Growth by Mergers

After virialization, both the DM halo and the stellar content are expected to grow because of merging events. To describe

these processes, we rely on the outcomes of N-body and hydro simulations, in particular, the Illustris project (see http://www.illustris-project.org/). As to the halo growth, the merger rates per bin of redshift z and halo mass ratio $\mu_{\rm H}$ can be described with the fitting formula originally proposed by Fakhouri & Ma (2008), Fakhouri et al. (2010) and Lapi et al. (2013),

$$\frac{dN_{\rm H,merg}}{dt\ d\mu_{\rm H}} = N_{\rm H}\, M_{\rm H,12}^{a}\, \mu_{\rm H}^{-b-2}\, e^{(\mu_{\rm H}/\tilde{\mu}_{\rm H})^{c}}\, \frac{d\delta_c}{dt}, \tag{49}$$

in terms of the descendant halo mass $M_{\rm H,12} = M_{\rm H}/10^{12}\, M_\odot$ and the linear threshold for collapse $\delta_c(z)$. Genel et al. (2010) determined the parameters entering the above expression from the Illustris-Dark simulations, finding $N_{\rm H} = 0.065$, $a = 0.15$, $b = -0.3$, $c = 0.5$, and $\tilde{\mu}_{\rm H} = 0.4$. The average halo mass growth $\langle \dot{M}_{\rm H\ merg}\rangle$ is obtained by multiplying the above expression by $\mu_{\rm H}/(1+\mu_{\rm H})$ and integrating over $\mu_{\rm H}$ from a minimum value $\mu_{\rm H,min}$; we use $\mu_{\rm H,min} \approx 10^{-5}$, which corresponds to include all mergers, since the contribution from smaller mass ratios to the halo mass growth is essentially negligible.

As to the stellar mass growth, Rodriguez-Gomez et al. (2015, 2016) inferred from the analysis of the full hydrodynamic Illustris simulation the fitting formula

$$\frac{dN_{\star,\rm merg}}{dt\ d\mu_\star} = N_\star(z_{\rm form}) M_{\star,10}^{a(z_{\rm form})} \times [1 + (M_\star/\tilde{M}_\star)^{d(z_{\rm form})}]\, \mu_\star^{b(z_{\rm form})+c\log M_{\star,10}} \tag{50}$$

in terms of the descendant stellar mass $M_{\star,10} = M_\star/10^{10}\, M_\odot$, where $\tilde{M}_\star = 2\times 10^{11}\, M_\odot$, $N_\star(z_{\rm form}) = N_0\,(1+z_{\rm form})^{N_1}$ with $\log N_0[\ {\rm Gyr}^{-1}] = -2.2287$ and $N_1 = 2.4644$, $a(z_{\rm form}) = a_0\,(1+z_{\rm form})^{a_1}$ with $a_0 = 0.2241$ and $a_1 = -1.1759$, $b(z_{\rm form}) = b_0\,(1+z_{\rm form})^{b_1}$ with $b_0 = -1.2595$ and $b_1 = 0.0611$, $c = -0.0477$, and $d(z_{\rm form}) = d_0\,(1+z_{\rm form})^{d_1}$ with $d_0 = 0.7668$ and $d_1 = -0.4695$. To obtain the average stellar mass growth $\langle \dot{M}_{\star,\rm merg}\rangle$ via mergers, we follow Rodriguez-Gomez et al. (2016) in multiplying the above expression by $\mu_\star/(1+3\,\mu_\star)$ and integrating over $\mu_\star$ from a minimum value $\mu_{\star\rm min} \approx 10^{-2}$; the latter value practically corresponds to include all relevant mergers, since the cumulative effect from those with smaller stellar mass ratios is negligible with respect to the stellar mass growth (see Rodriguez-Gomez et al. 2016). Note that we exploit the above merging rates from Illustris but not the related prescriptions for in situ star formation, which are instead based on our framework; this approach is aimed at reproducing the halo-to-stellar mass ratio at different redshifts (see Section 4.2 and Figure 5).

During each time step dt after halo formation at $z_{\rm form}$ until the observation redshift $z_{\rm obs}$, the halo and stellar mass are increased by the amounts $\langle \dot{M}_{\rm merg,H}\rangle\, dt$ and $\langle \dot{M}_{\rm merg,star}\rangle\, dt$, respectively. To have a grasp on such mass additions, in Figure 4, we illustrate the growth of halo and stellar mass via mergers as a function of the descendant final masses. Specifically, we show the outcomes at observation redshifts $z_{\rm obs} = 0$, 2, 4, and 6 (color-coded) and different formation redshifts $z_{\rm form} = z_{\rm obs} + 1.5$, $z_{\rm obs} + 2.5$, and $z_{\rm obs} + 3.5$ (line style–coded). Plainly, at a given observation and formation redshift, the amount of relative mass addition by mergers increases with the descendant mass, while at a given descendant mass and observation redshift, the mass additions increase for increasing formation redshift; in addition, the halo mass addition depends weakly on the observation redshift, while the stellar mass addition appreciably increases for decreasing $z_{\rm obs}$. Typically, the halo mass increase at $z_{\rm obs} \approx 0$ for a descendant halo mass $M_{\rm H} \approx 10^{13}\, M_\odot$ formed at $z_{\rm form} \approx 2.5$ amounts to a factor of $\sim$3; correspondingly, the stellar mass increase at $z_{\rm obs} \approx 0$ for a galaxy with descendant stellar mass $M_\star \approx 3\times 10^{11}\, M_\odot$ formed at $z_{\rm form} \approx 2.5$ amounts to $\sim$50%.

3.5. Average Over Formation Redshift

In order to derive the statistical properties of the galaxy population concerning a quantity $\mathcal{Q}$ (e.g., halo mass, SFR, stellar mass), we proceed as follows. We exploit the analytic solutions of Section 2 for the evolution of individual galaxies with different formation redshift $z_{\rm form}$ and halo masses $M_{\rm H}$ at formation (the halo mass at $z_{\rm obs}$ is larger because of mass addition by mergers; see previous section) to obtain $\mathcal{Q}(\tau|M_{\rm H}, z_{\rm form})$. Given an observation redshift $z_{\rm obs} \lesssim z_{\rm form}$, we pick up the value of $\mathcal{Q}$ at $\tau = t_{z_{\rm obs}} - t_{z_{\rm form}}$, where t_z is the cosmic time at redshift z. Finally, we perform the average over different formation redshifts to get

$$\langle \mathcal{Q}\rangle(M_{\rm H}, z_{\rm obs}) \propto \int_{z_{\rm obs}}^{\infty} dz_{\rm form}\, \frac{d^2N_{\rm H}}{d\log M_{\rm H}\, dz_{\rm form}}\, \mathcal{Q} \times (t_{z_{\rm obs}} - t_{z_{\rm form}}|M_{\rm H}, z_{\rm form}), \tag{51}$$

where $d^2N_{\rm H}/d\log M_{\rm H}\, dz_{\rm form}$ is the halo formation rate computed via the excursion set framework and checked against N-body simulations by Lapi et al. (2013; see also Lacey & Cole 1993; Kitayama & Suto 1996; Moreno et al. 2009; Giocoli et al. 2012). The normalization constant in Equation (51) is clearly the same integral without $\mathcal{Q}$, and the 1σ variance is computed as $\sigma_{\mathcal{Q}} = \sqrt{\langle \mathcal{Q}^2\rangle - \langle \mathcal{Q}\rangle^2}$.

To compute the formation rate, one needs the halo mass function, i.e., the comoving number density of the halo per halo mass bin, as provided by state-of-the-art N-body simulations; we adopt the determination by Tinker et al. (2008; see also Watson et al. 2013; Bocquet et al. 2016; Comparat et al. 2017, 2019). Since we are mainly concerned with the properties of ETGs residing at the centers of halos, we actually exploit the galaxy halo mass function, i.e., the mass function of halos hosting one individual galaxy (though the difference with respect to the halo mass function emerges only for $z \lesssim 1$ and $M_{\rm H} \gtrsim$ several $10^{13}\, M_\odot$). This can be built up from the overall halo mass function by adding to it the contribution of subhalos and by probabilistically removing from it the contribution of halos corresponding to galaxy systems via halo occupation distribution modeling; we refer the reader to Appendix A of Aversa et al. (2015) for details on such a procedure.

4. Results

We now present, compare with recent data, and discuss a bunch of results from our analytic solutions applied to ETGs and their star-forming progenitors.

4.1. Time Evolution of Individual Galaxies

We start by presenting the evolution with galactic age τ of the relevant spatially averaged quantities described by our analytic solutions: infalling gas mass, cold gas mass, stellar mass, gas and stellar metallicity, and dust mass. In Figures 2

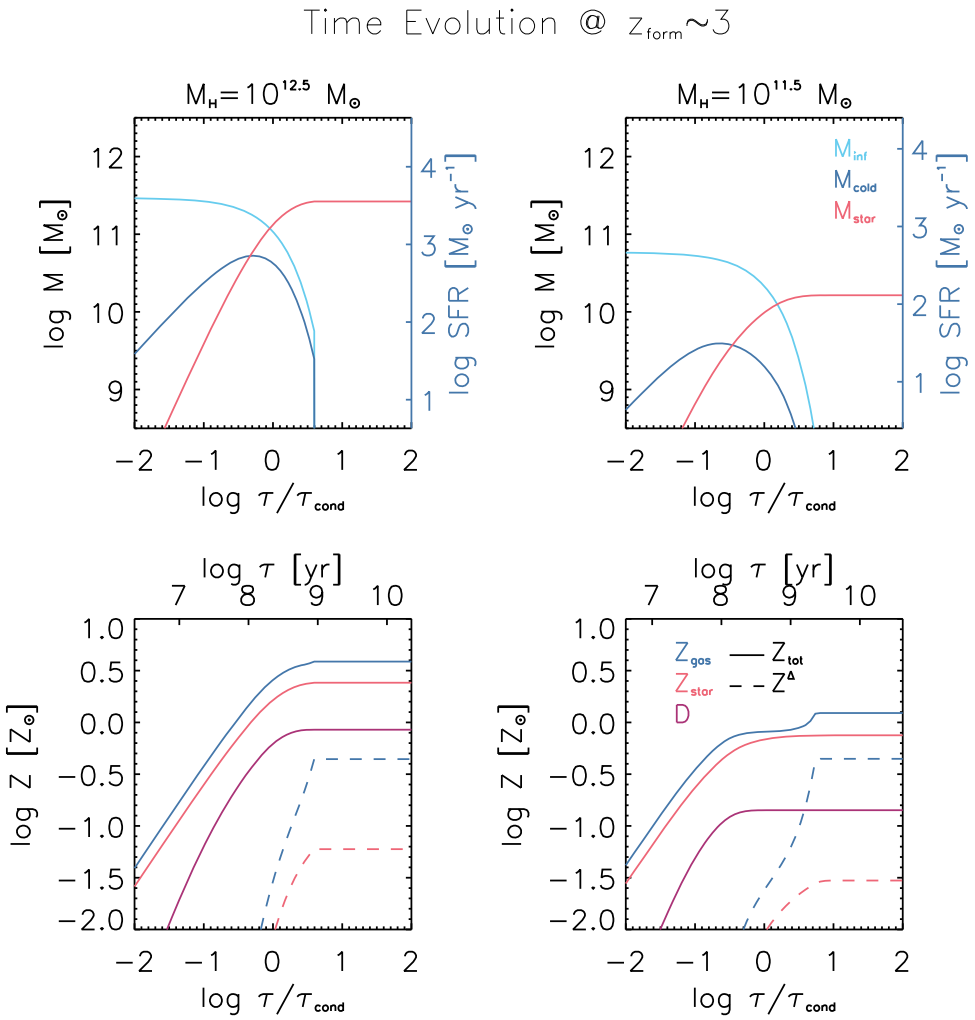

Figure 2. Evolution of the mass components (top panels) and metallicity and dust-to-gas ratio (bottom panels) as a function of galactic age (normalized to the condensation timescale $\tau_{\rm cond}$ or in absolute units of yr) for galaxies hosted in halos with mass $M_{\rm H} = 10^{12.5}\,M_{\odot}$ (left panels) and $M_{\rm H} = 10^{11.5}\,M_{\odot}$ (right panels) at formation redshift $z_{\rm form} = 3$. To highlight in situ evolution, halo and stellar mass additions by mergers are switched off. In the top panels, cyan lines refer to the infalling mass $M_{\rm inf}$, orange lines to the stellar mass $M_{\star}$ (actually the integral of the SFR), and blue lines to the cold gas mass $M_{\rm cold}$ (the corresponding SFR values $\dot{M}_{\star} = s\,M_{\rm cold}/\tau_{\rm cond}$ can be read on the right y-axis). In the bottom panels, blue lines refer to the cold gas metallicity $Z_{\rm cold}$, orange lines to the stellar metallicity $Z_{\star}$, and red lines to the dust-to-gas mass ratio D; moreover, solid lines are for the total metallicity, while dashed lines highlight the contribution from delayed metals.

and 3, we illustrate representative galaxies with different halo masses, $M_{\rm H} = 10^{12.5}$ and $10^{11.5}\,M_{\odot}$, formed at different redshifts, $z_{\rm form} = 3$ and 6.

The infalling gas mass decreases exponentially with the galactic age as it condenses in the cold gas component, which in turn feeds star formation; on the other hand, both components are affected by SN feedback. The balance of these processes makes the cold gas mass (and hence the SFR) slowly grow at early times, attain a maximum, and then decrease exponentially; correspondingly, the stellar component increases almost linearly and then saturates. In massive halos with $M_{\rm H} \gtrsim 10^{12}\,M_{\odot}$, star formation is abruptly quenched by BH feedback soon after $\tau_{\rm burst} \sim$ a few 10^8 yr, while the residual gas mass is removed; conversely, in less massive halos, $M_{\rm H} \lesssim 10^{12}\,M_{\odot}$ BH feedback is inactive, so star formation can proceed for longer times, $\tau_{\rm burst} \gtrsim$ a few 10^9 yr, until the gas reservoir gets exhausted. This differential behavior is induced by the dependence of $\tau_{\rm burst}$ on halo mass, as specified by Equation (48), and phenomenologically renders the well-known downsizing behavior. In galaxy halos formed earlier, the typical SFRs are larger and the accumulated stellar masses higher.

The metallicity in cold gas and stars rises almost linearly, so after a few 10^7 yr, it attains values above $\gtrsim Z_{\odot}/10$; note that this rapid increase is particularly relevant for the metal enrichment of high-redshift galaxies and QSO hosts (see Maiolino et al. 2005; Wang et al. 2008; Omont et al. 2013; Michalowski 2015; Willott et al. 2015; Venemans et al. 2018). In massive halos, the metallicity saturates after a time, a few 10^8 yr, to (super)solar values, and the contribution by delayed metals from Type Ia SNe to the stellar metallicity is minor, since the BH feedback stops the star formation before any significant pollution. On the other hand, in low-mass halos, only subsolar values are attained, and the contribution from delayed metals becomes relatively more important, especially at old ages; this differential behavior in the relative fraction of instantaneous and delayed metals will be at the origin of the observed α-enhancement in massive galaxies. The dust-to-gas ratio follows a behavior similar to the metal enrichment, with a quite rapid growth within $\sim 10^8$ yr driven mainly by accretion onto preformed core grains, up to a saturation value that can be close to unity in massive halos, while it stays $\lesssim 0.3$ in smaller ones. We stress that the evolution of metals and dust is quite

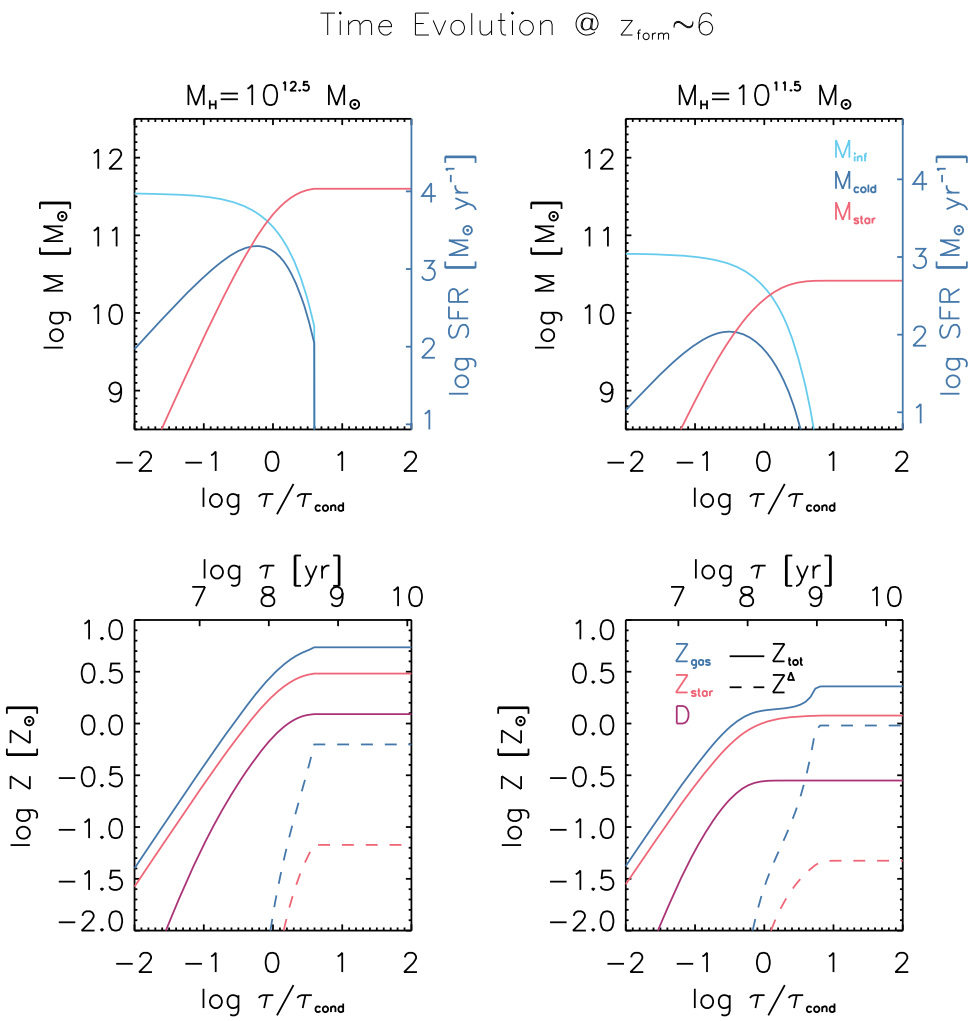

Figure 3. Same as previous figure at formation redshift $z_{\rm form} = 6$.

rapid and, being mainly related to in situ processes, weakly dependent on redshift; this could be important for detecting primordial galaxies at $z \gtrsim 6$ in future wide-area IR surveys, which will be routinely achievable with ALMA and the advent of the *James Webb Space Telescope* (*JWST*; see De Rossi & Bromm 2019).

4.2. Star Formation Efficiency

In Figure 5, we show the star formation efficiency $f_\star \equiv M_\star/f_b\, M_{\rm H}$, namely, the fraction of initial baryonic mass converted into stars, as a function of the stellar mass for different observation redshifts $z_{\rm obs} = 0$, 2, 4, and 6 (color-coded); the shaded areas illustrate the 1σ scatter associated with the average over formation redshifts. The star formation efficiency $f_\star$ is found to be a nonmonotonic function of the stellar mass $M_\star$, with a maximum value of 20%–30% slowly increasing with redshift around $M_\star \simeq 10^{11}\, M_\odot$ and a decrease to values less than 10% for $M_\star \sim$ a few $10^9\, M_\odot$ and $M_\star \simeq 10^{12}\, M_\odot$; all in all, star formation in galaxies is a very inefficient process.

Such behavior is easily understood in terms of infall/condensation and feedback processes. At small masses, infall and condensation are efficient ($f_{\rm inf} \approx 1$), but star formation is regulated by outflows from SNe and stellar winds; conversely, at high masses, infall and condensation become less efficient ($f_{\rm inf} \lesssim 1$), and star formation is also hindered by BH feedback. All in all, the maximum value of the star formation efficiency occurs at a mass corresponding approximately to the transition between the stellar and BH feedback (see Shankar et al. 2006; Moster et al. 2013; Aversa et al. 2015).

Our result at $z_{\rm obs} \approx 0$ is compared with the local data for ETGs from various authors determined via weak lensing (see Velander et al. 2014; Hudson et al. 2015; Rodriguez-Puebla et al. 2015; Mandelbaum et al. 2016) and satellite kinematics (see More et al. 2011; Wojtak & Mamon 2013), while the outcome at $z \approx 2$ should be compared with the estimates by Burkert et al. (2016) via Hα data and mass profile modeling. We find very good agreement in normalization and scatter within the still-large observational uncertainties. Our results as a function of redshift are also similar, within a factor of 2, to the determinations via an abundance-matching technique by Behroozi et al. (2013), Moster et al. (2013), Aversa et al. (2015), and Lapi et al. (2017).

We stress that the similarity of the efficiency at $z \approx 2$ to the local values is indicative that star formation is mainly an in situ process (see Lilly et al. 2013; Moster et al. 2013; Aversa et al. 2015; Mancuso et al. 2016a); actually, the difference in $f_\star$ between these redshifts is mainly driven by the increase in the stellar and halo mass due to late-time mergers.

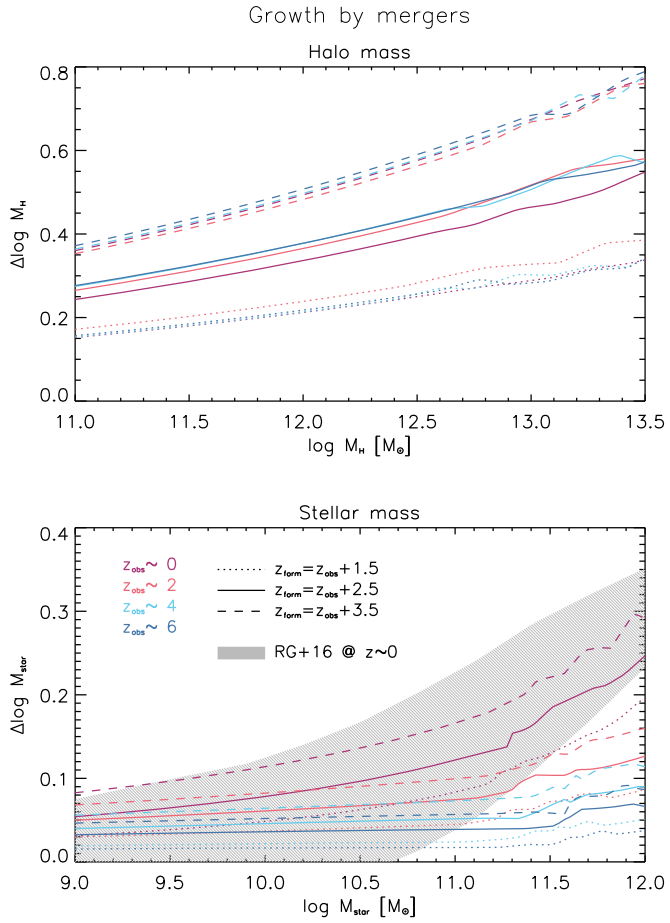

Figure 4. Growth of the halo mass (top panel) and stellar mass (bottom panel) by mergers as a function of the final halo and stellar masses, respectively. We illustrate the outcomes at observation redshifts $z_{\rm obs} = 0$ (red), 2 (orange), 4 (cyan), and 6 (blue) for different formation redshifts $z_{\rm form} = z_{\rm obs} + 1.5$ (dotted), $z_{\rm obs} + 2.5$ (solid), and $z_{\rm obs} + 3.5$ (dashed). For $z_{\rm obs} = 0$, we also show the typical stellar mass growth via mergers from the Illustris simulation by Rodriguez-Gomez et al. (2016; gray shaded area).

4.3. Galaxy MS

In Figure 6, we present our results concerning the so-called MS of star-forming galaxies (e.g., Daddi et al. 2007; Elbaz et al. 2007; Noeske et al. 2007; Rodighiero et al. 2011, 2015; Speagle et al. 2014; Whitaker et al. 2014; Schreiber et al. 2017; Tacchella et al. 2018b; Popesso et al. 2019), namely, the relation between the SFR and stellar mass at different observation redshifts, $z_{\rm obs} = 2$, 4, and 6 (color-coded). The outcomes at $z \sim 2$ are in pleasing agreement with the observational determination from the large statistics of mass-selected galaxy samples by Rodighiero et al. (2015); this further substantiates our solutions for the time evolution of the star formation and stellar mass in individual galaxies.

To highlight the relevance of observational selections different from that based on stellar mass, in Figure 6, we also report data points for individual, far-IR-selected galaxies by Koprowski et al. (2016), Ma et al. (2016), and Negrello et al. (2014), along with Dye et al. (2015), da Cunha et al. (2015), and Dunlop et al. (2017), mainly at redshifts $z \sim 1$–4. An appreciable fraction of the individual, far-IR-selected galaxies around $z \sim 2$ (highlighted by dots within open symbols) lie above the MS, i.e., at SFR values higher than expected on the basis of the average relationship at a given $M_\star$. These off-MS objects can be simply interpreted (see

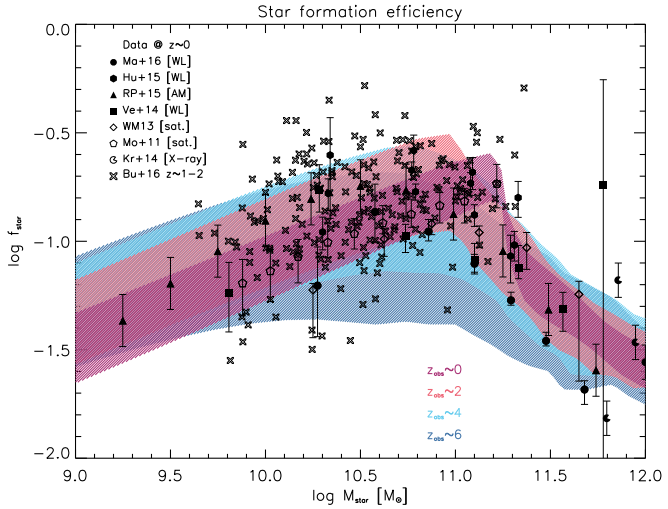

Figure 5. Star formation efficiency $f_\star = M_\star/f_{\rm b}\,M_H$ vs. stellar mass $M_\star$ at different observation redshifts $z \approx 0$ (red), 2 (orange), 4 (cyan), and 6 (blue); the shaded areas illustrate the 1σ variance associated with the average over different formation redshifts. Data points are from Mandelbaum et al. (2016; circles), Hudson et al. (2015; hexagons), and Velander et al. (2014; squares) via weak lensing; Rodriguez-Puebla et al. (2015; triangles) via subhalo abundance matching; Wojtak & Mamon (2013; diamonds) and More et al. (2011; pentagons) via satellite kinematics; Kravtsov et al. (2018, pacmans) via X-ray observations of BCGs; and Burkert et al. (2016; crosses) via mass profile modeling of galaxies at $z \sim 1$–2. If not explicitly indicated, error bars are ≈0.25 dex.

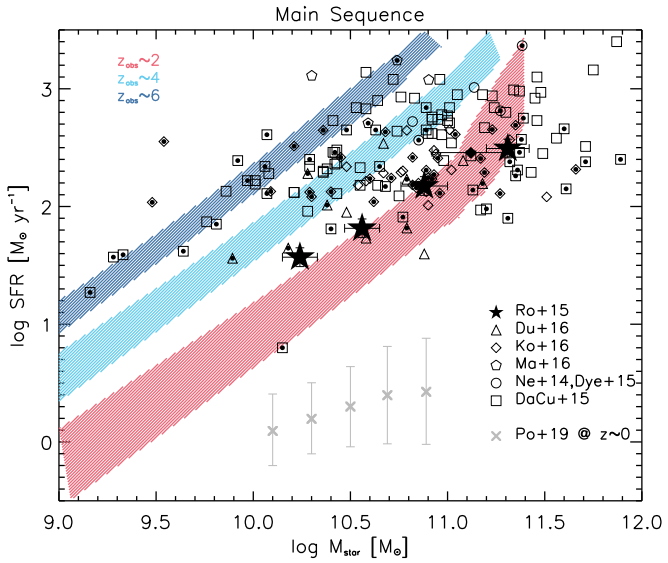

Figure 6. The SFR vs. stellar mass $M_\star$, alias the MS of star-forming galaxies, at different observation redshifts $z \approx 2$ (orange), 4 (cyan), and 6 (blue); the shaded areas illustrate the 1σ variance associated with the average over different formation redshifts. The black filled stars are the observational determinations of the MS at $z \sim 2$ based on the statistics of large mass-selected samples by Rodighiero et al. (2015). The other symbols (error bars omitted for clarity) refer to far-IR data for individual objects at $z \sim 1$–4 (those in the range $z \sim 1.5$–2.5 are marked with a dot) by Dunlop et al. (2017; triangles), Koprowski et al. (2016; diamonds), Ma et al. (2016; pentagons), Negrello et al. (2014), Dye et al. (2015; circles), and da Cunha et al. (2015; squares); for reference, the determination at $z \approx 0$ by Popesso et al. (2019; crosses) is also reported.

Lapi et al. 2017; Mancuso et al. 2016b) as galaxies caught in an early evolutionary stage and still accumulating their stellar mass. Thus, young star-forming galaxies are found to be preferentially located above the MS or, better, to the left of it. As time goes by

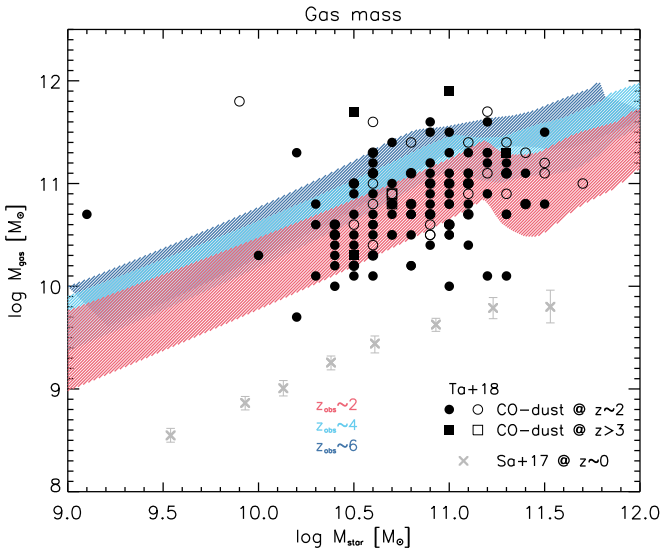

Figure 7. Gas mass $M_{\rm gas}$ vs. stellar mass $M_\star$ at different observation redshifts, $z \approx 2$ (orange), 4 (cyan), and 6 (blue); the shaded areas illustrate the 1σ variance associated with the average over different formation redshifts. Data points are from Tacconi et al. (2018); circles represent objects at $z \sim 2$, while squares stand for galaxies at redshifts $z \gtrsim 3$. Filled symbols refer to gas mass estimates from CO lines and open symbols from dust far-infrared/submillimeter continuum. Error bars on data points (omitted for clarity) are of order ≈0.25 dex; for reference, data at $z \approx 0$ from Saintonge et al. (2017; crosses) are also reported.

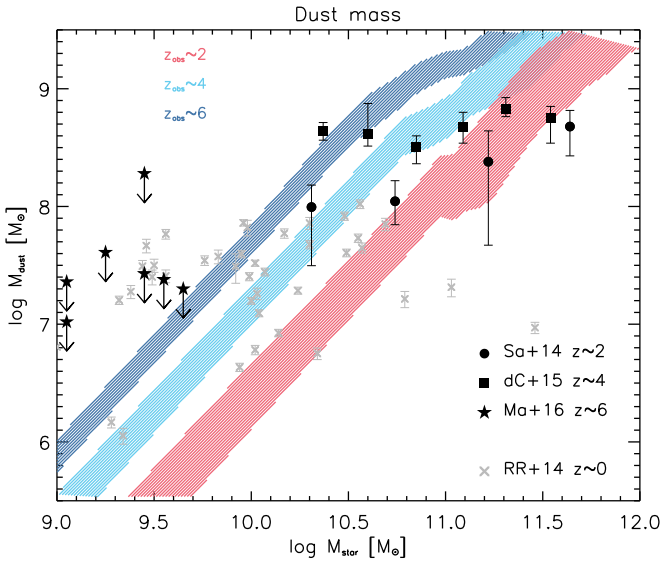

Figure 8. Dust mass $M_{\rm dust}$ vs. stellar mass $M_\star$ at different observation redshifts, $z \approx 2$ (orange), 4 (cyan), and 6 (blue); the shaded areas illustrate the 1σ variance associated with the average over different formation redshifts. Data points are from Santini et al. (2014; circles) at $z \sim 2$, da Cunha et al. (2015; squares) at $z \sim 4$, and Mancini et al. (2015; stars) $z \sim 6$ (upper limits only); for reference, measurements at $z \approx 0$ by Remy-Ruyer et al. (2014; crosses) are also reported.

and the stellar mass increases, the galaxy moves toward the average MS relationship, around which it will spend most of its lifetime. Afterward, the SFR is quenched by feedback, and the galaxy will then evolve passively to become a local early type; it will then populate a region of the SFR–versus–stellar mass diagram that is substantially below the MS. These loci of red-and-dead galaxies are indeed observed locally (see Renzini & Peng 2015) and start to be pinpointed even at increasing redshift (see Man et al. 2016). For reference, in Figure 6, we also report the determination at $z \approx 0$ by Popesso et al. (2019), which is mainly representative of the local disk-dominated galaxies (not included in our framework); typically, these have star formation histories prolonged over several Gyr and continue to form stars, though at rather low rates of a few $M_\odot\ {\rm yr}^{-1}$, even toward $z \approx 0$.

The overall redshift evolution of the MS for ETGs and their progenitors is consistent with a scenario that traces the bulk of the star formation in galaxies back to local, in situ condensation processes. Specifically, at higher z and in massive galaxies, the interstellar medium is, on average, denser, and the condensation/star formation timescales are shorter. Thus, star formation in a galaxy of a given stellar mass is higher, causing the MS locus to shift upward. We stress that, moving toward higher redshift, the fraction of off-MS objects decreases appreciably; this is because, given the evolution of the SFR function and the shorter age of the universe, it is more and more difficult to spot galaxies of appreciably different ages and featuring very high SFRs.

4.4. Gas Mass

In Figure 7, we illustrate the relationship between the gas mass $M_{\rm gas}$ and the stellar mass $M_\star$ for different observation redshifts, $z_{\rm obs} \sim 2$, 4, and 6 (color-coded). Over most of the stellar mass range, the gas mass increases monotonically; the relationship holds up to $M_\star \sim 10^{11}\,M_\odot$, where a decrease in the gas mass is enforced, since the infall/condensation processes become inefficient. As to the redshift evolution, the gas mass is slightly higher for star-forming galaxies observed at earlier epochs; this can be traced back to the fact that objects observed at higher redshift are, on average, younger and expected to have converted less gas into stars. Note that at $z_{\rm obs} = 0$, the descendants of these star-forming galaxies, i.e., local ETGs, have very small gas reservoirs, since most of the gas has been consumed via star formation and/or ejected by feedback events. In fact, the $z \approx 0$ determination from Saintonge et al. (2017), reported as a reference, refers mainly to disk-dominated galaxies that are gas-rich and still star-forming in the local universe.

Our results for star-forming ETG progenitors are compared with the gas mass estimates from Tacconi et al. (2018) from ALMA data for a large sample of star-forming galaxies at redshifts $z \sim 1$–4; the agreement with the data is good in normalization, scatter, and redshift evolution, although still-large observational uncertainties hinder a more detailed comparison.

4.5. Dust Mass

In Figure 8, we show the dust mass $M_{\rm dust}$ as a function of the stellar mass $M_\star$ for different observation redshifts, $z_{\rm obs} \sim 2$, 4, and 6 (color-coded). A direct relationship is expected, since both dust and stellar mass are strictly related to the SFR. In fact, the dust mass is produced in SN ejecta/stellar winds that are more efficient when the SFR is higher; the latter also favors metal-rich environments, in turn triggering efficient growth of dust grains by accretion. At a given stellar mass, higher-redshift galaxies are expected to produce slightly larger amounts of dust; the trend can be traced back to their denser environment, in turn yielding shorter star formation timescales.

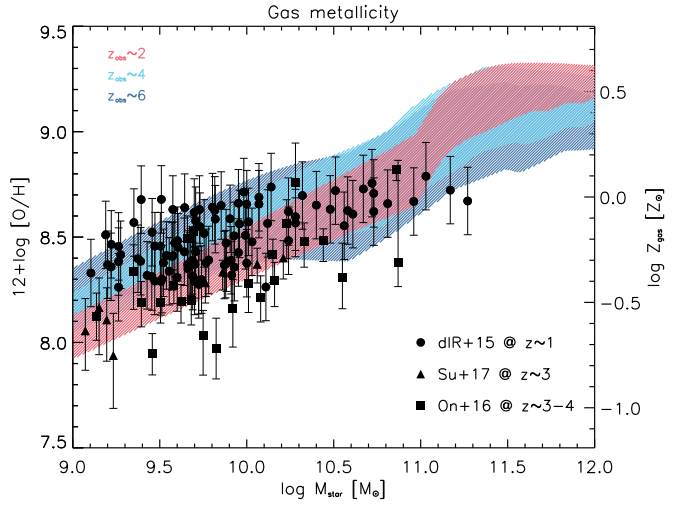

Figure 9. Gas metallicity $Z_{\rm gas}$ vs. stellar mass $M_\star$ at different observation redshifts, $z \approx 2$ (orange), 4 (cyan), and 6 (blue); the shaded areas illustrate the 1σ variance associated with the average over different formation redshifts. Data points are from de los Reyes et al. (2015; circles) at $z \sim 1$, Suzuki et al. (2017; triangles) at $z \sim 3$, and Onodera et al. (2016; squares) at $z \sim 3$–4. All gas metallicities have been converted to PP04O3N2 calibration.

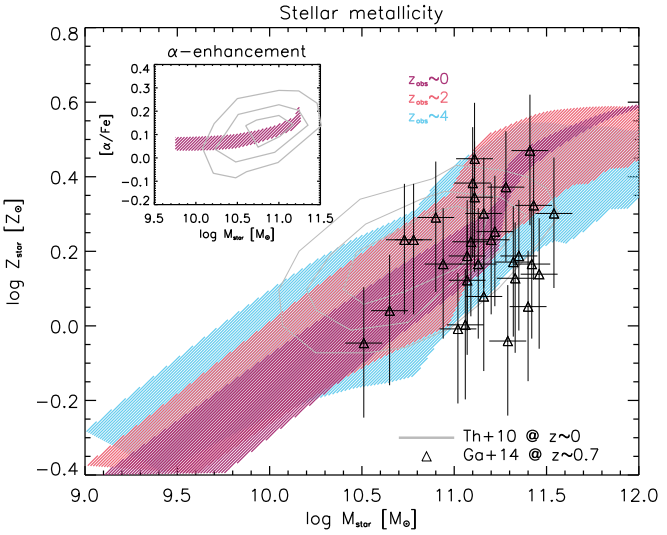

Figure 10. Stellar metallicity $Z_\star$ vs. stellar mass $M_\star$ at different observation redshifts, $z \approx 0$ (red), 2 (orange), and 4 (cyan); the shaded areas illustrate the 1σ variance associated with the average over different formation redshifts. Data for SDSS samples of local ETGs are from Thomas et al. (2010; solid contours), and data for individual galaxies at $z \sim 0.7$ are from Gallazzi et al. (2014; triangles). Inset: as above for α-element–to–iron abundance ratio [α/Fe] vs. stellar mass $M_\star$ at observation redshift $z \approx 0$ (red).

Our results for star-forming ETG progenitors are in good agreement with the observational estimates by Santini et al. (2014) at $z \sim 2$ from stacked far-IR photometry, da Cunha et al. (2015) at $z \sim 4$ from submillimeter SED modeling, and Mancini et al. (2015) from upper limits to thermal dust emission in $z \sim 6$ star-forming galaxies. For reference, we also report the $z \approx 0$ dust mass estimates by Remy-Ruyer et al. (2014), mainly referring to disk-dominated galaxies, which are still star-forming and moderately gas-rich, even in the local universe.

4.6. Gas Metallicity

In Figure 9, we present the mass–metallicity relationship (see Tremonti et al. 2004; Erb et al. 2006; Maiolino et al. 2008; Steidel et al. 2014; Zahid et al. 2014; de los Reyes et al. 2015; Sanders et al. 2015; Faisst et al. 2016; Onodera et al. 2016; Suzuki et al. 2017), i.e., the relation between the gas metallicity $Z_{\rm gas}$ of the cold gas and the stellar mass $M_\star$ at different observation redshifts $z_{\rm obs} \sim 2$, 4, and 6 (color-coded). The gas metallicity shows an increasing behavior as a function of the final stellar mass, related to the more efficient production of metals in galaxies with higher SFRs, that will also yield larger stellar masses; the corresponding redshift evolution is negligible, being the gas metallicity essentially related to in situ processes.

Our results are in agreement with gas metallicity estimates (traced mainly by oxygen abundance and converted to PP04O3N2 calibration; see Kewley & Ellison 2008) from strong rest-frame optical emission lines in UV/optically selected star-forming galaxies by de los Reyes et al. (2015), Onodera et al. (2016), and Suzuki et al. (2017) spanning the redshift interval $z \sim 1$–4.

4.7. Stellar Metallicity and α-enhancement

In Figure 10, we illustrate the stellar mass–metallicity relationship (see Thomas et al. 2005, 2010; Gallazzi et al. 2006, 2014; Johansson et al. 2012), i.e., the relationship between the stellar metallicity $Z_\star$ and the stellar mass $M_\star$ at different observation redshifts, $z_{\rm obs} = 0$, 2, and 4 (color-coded). The stellar metallicity increases monotonically with stellar mass, mirroring the gas metallicity behavior (see Figure 9). This is because massive galaxies are characterized, on average, by higher SFRs that imply larger stellar masses and metal production. Moreover, in low-mass galaxies, the depletion of metals by stellar feedback is enhanced due to the shallower potential wells associated with the host halos. Contrariwise, high-mass galaxies can retain greater amounts of chemical-enriched gas that could be converted and locked into new metal-rich stars, resulting in a higher stellar metallicity. The evolution in redshift is minor, as the stellar metallicity is mainly determined by in situ star formation processes in the central regions; if any, at higher z and a given stellar mass, the stellar metallicity increases slightly, since the average SFR is larger.

Our results are in agreement with measurements of stellar metallicity in local ETGs by Thomas et al. (2010) from the SDSS and estimates by Gallazzi et al. (2014) at $z \sim 0.7$, which are broadly consistent with the local relationship within their large uncertainties and intrinsic variance. Note that a few other works attempted to derive stellar metallicity out to $z \sim 3$ in star-forming galaxies, but these analyses are based on rest-frame UV absorption features, which are good tracers only of the youngest stellar populations (e.g., Halliday et al. 2008; Sommariva et al. 2012).

In the inset of Figure 10, we show the α-enhancement (see Thomas et al. 2005, 2010; Johansson et al. 2012), i.e., the local α-element–to–iron abundance ratio [α/Fe] as a function of galaxy stellar mass $M_\star$. At small stellar masses, $M_\star \lesssim 10^{10}\,M_\odot$, an almost constant [$\alpha$/Fe] ≈ 0.05 is found, while in moving toward higher masses, [α/Fe] increases up to a value of $\sim$0.25. This trend can be strictly related to the diverse star formation histories characterizing small and high-mass galaxies. In particular, in massive galaxies, BH feedback is able to quench the star formation and deplete the residual gas mass within a fraction of Gyr, well before Type Ia SNe can pollute the ISM

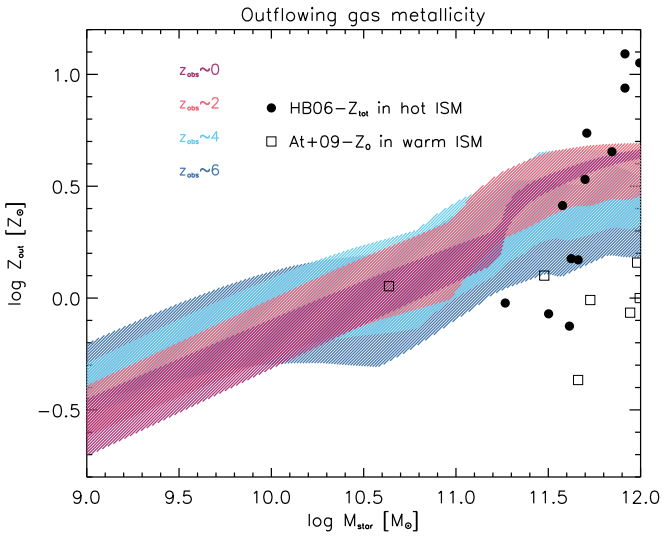

Figure 11. Outflowing gas metallicity $Z_{\rm out}$ vs. stellar mass $M_\star$ at different observation redshifts, $z \approx 0$ (red), 2 (orange), 4 (cyan), and 6 (blue); the shaded areas illustrate the 1σ variance associated with the average over different formation redshifts. Data points referring to total α-element abundances in the hot ISM of local ETGs are from Humphrey & Buote (2006; circles), and those referring to oxygen abundance in the warm ISM of local ETGs are from Athey & Bregman (2009; squares); the latter may be considered lower limits to the total outflowing gas metallicity. Error bars on data points of order $\lesssim$1 dex have been omitted for clarity.

with substantial iron content; this results in an underabundance of iron with respect to α-elements in the stellar component, which in turn causes an excess in [α/Fe]. Contrariwise, in low-mass galaxies, star formation proceeds longer, and Type Ia SNe have time to enrich the ISM and stars with a relatively larger amount of iron. We find a good agreement of our result with the observed α-enhancement of local ETGs, as estimated by Thomas et al. (2010).

4.8. Outflow Metallicity

In Figure 11, we illustrate the metallicity of the outflowing material $Z_{\rm out}$ as a function of the stellar mass $M_\star$ for different observation redshifts, $z \sim 0$, 2, 4, and 6 (color-coded). Relevant measurements of the metallicity concern the warm (temperatures 10^4 K; e.g., Caon et al. 2000; Ferrari et al. 2002; Athey & Bregman 2009) and hot (temperatures 10^6–10^7 K; see Loewenstein & Mathews 1991; Mathews & Brighenti 2003; Humphrey & Buote 2006) gas in local massive ETGs, as the outflowing chemical-enriched gas has possibly been retained in the host halo potential well. As to the hot gas, we report estimates by Humphrey & Buote (2006), who exploited X-ray observations to derive the iron amount and its abundance ratios with other elements in the hot ISM. As to the warm gas, we report the estimates by Athey & Bregman (2009), who determined a lower limit to the ISM metallicity of their ETG sample via oxygen emission lines.

The data points are clustered in the high-mass end of the plot and are consistent with our results at $z_{\rm obs} \approx 0$, albeit their large uncertainties (omitted for clarity but amounting to about 0.5 dex) do not allow us to draw a strong conclusion. Finally, it is worth noticing that the solar or even supersolar metallicities found in the hot and warm medium of local ETGs indicate that the ISM metals have a mostly in situ, internal origin. As also stressed by Humphrey & Buote (2006) and Athey & Bregman (2009), a significant external contribution from cosmic-scale primordial gas or minor mergers should imply a significant dilution of the ISM in ETGs, with an ensuing reduction in metallicity. There is a caveat, however: the issue is still debated, given the still-large observational uncertainties in the ISM metallicity determinations.

5. Summary

We have presented a set of new analytic solutions aimed at describing the spatially averaged evolution of the gas/stellar/dust mass and metal content in a star-forming galaxy hosted within a dark halo of a given mass and formation redshift (see Section 2 and Figures 2 and 3). The basic framework pictures the galaxy as an open, one-zone system comprising three interlinked mass components: a reservoir of warm gas subject to cooling and condensation toward the central regions, cold gas fed by infall and depleted by star formation and stellar feedback (Type II SNe and stellar winds), and stellar mass partially restituted to the cold phase by stars during their evolution. The corresponding metal enrichment history of the cold gas and stellar mass is self-consistently computed using as input the solutions for the evolution of the mass components; the metal equations include effects of feedback, astration, instantaneous production during star formation, and delayed production by Type Ia SNe, possibly following a specified DTD. Finally, the dust mass evolution takes into account the formation of grain cores associated with star formation and grain mantles due to accretion onto preexisting cores; astration of dust by star formation and stellar feedback and spallation by SN shock waves are also included.

We have then applied our analytic solutions to describe the formation of ETGs and the evolution of their star-forming progenitors (see Section 3). To this purpose, we have supplemented our solutions with a couple of additional ingredients: (i) specific prescriptions for parameter setting, inspired by in situ galaxy-BH coevolution scenarios for ETG formation, and (ii) estimates of the average halo and stellar mass growth by mergers, computed on the basis of the merger rates from state-of-the-art numerical simulations (see Figure 4). We then derive a bunch of fundamental relationships involving spatially averaged quantities as a function of the observed stellar mass: star formation efficiency (see Figure 5), SFR (see Figure 6), gas mass (see Figure 7), dust mass (see Figure 8), gas metallicity (see Figure 9), stellar metallicity and [α/Fe] ratio (see Figure 10), and outflowing gas metallicity (see Figure 11). We compare these relationships with the data concerning local ETGs and their high-z star-forming progenitors, finding a pleasing overall agreement (see Section 4). We remark that a major value of our approach is to reproduce, with a unique set of physically motivated parameters, a wealth of observables concerning ETGs and their progenitors.

Another straightforward application of our solutions would be the description of the spatially averaged properties for local disk-dominated (e.g., spiral) galaxies. On the one hand, this will just require different prescriptions for parameter setting with respect to ETG progenitors. In a nutshell, we expect appreciably longer condensation/star formation timescales of the order of several Gyr and a minor role for BH feedback; this will originate a prolonged star formation history to low SFR levels and appreciable dilution from infalling matter, in turn implying slower accumulation of stellar mass, metals, and dust. On the other hand, additional processes like galactic fountains, differential winds, stellar mixing, and multizonal effects may

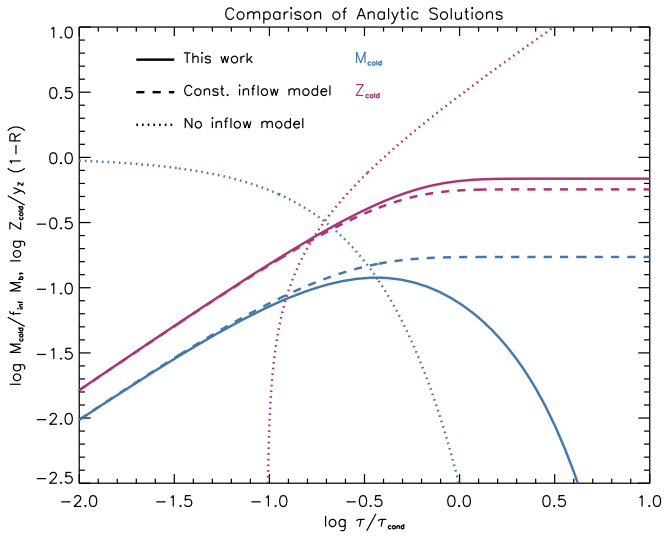

Figure 12. Comparison of the analytic solutions developed in this work (solid lines) with the classical no-inflow/closed/leaky-box model (dotted lines) and constant-inflow/gas-regulator model (dashed lines); see the Appendix for more details. Blue lines illustrate the time evolution of the cold gas mass $M_{\rm cold}/f_{\rm inf}\,M_{\rm b}$, and red lines illustrate that of the cold gas metallicity $Z_{\rm cold}/y_Z(1-\mathcal{R})$. For a sensible comparison, we have adopted values of the relevant parameters $s\approx 3$ and $\gamma\approx 2$ that are apt for a galaxy hosted in a halo with mass $M_{\rm H}\approx 10^{12}\,M_\odot$ formed at $z_{\rm form}\approx 3$.

play a relevant role in local spirals; this will require the basic framework presented in Section 2 to become more complex and the search for realistic analytic solutions more challenging. We will pursue this program in a forthcoming paper.

To sum up, the analytic solutions provided here are based on idealized, albeit nontrivial, descriptions of the main physical processes regulating galaxy formation on a spatially average ground that go beyond simple approaches to the history of star formation and chemical enrichment, like the closed/leaky-box or gas-regulator models (see the Appendix and Figure 12). Yet our solutions are simple enough to easily disentangle the roles of the main physical processes at work, allow a quick exploration of the parameter space, and make transparent predictions on spatially averaged quantities. All in all, our analytic solutions may provide a basis for improving the (subgrid) physical recipes implemented in theoretical approaches and numerical simulations and can offer a benchmark for interpreting and forecasting current and future observations with multiband coverage that will become routinely achievable even at high redshift, e.g., via targeted observations with ALMA and dedicated surveys with the *JWST*.

We acknowledge the anonymous referee for a constructive report. We thank A. Bressan, A. Feltre, D. Donevski, and G. Rodighiero for helpful discussions. This work has been partially supported by PRIN MIUR 2017 prot. 20173ML3WW 002, Opening the ALMA window on the cosmic evolution of gas, stars and supermassive black holes. A.L. acknowledges the MIUR grant "Finanziamento annuale individuale attivitá base di ricerca."

Appendix
Comparison with Classic Analytic Models

In this appendix, we compare our new analytic solutions with classic analytic models, extensively adopted to describe the spatially averaged behavior of star-forming galaxies. We focus on two classes of models that have as limiting cases the classical closed-box and gas-regulator (or bathtube) solutions.

A.1. No-inflow Models and the Leaky/Closed-box Solution

A class of simple analytic models can be obtained by imposing no inflow of gas. The relevant equations describing the evolution of gas mass and metallicity can be written as

$$\begin{cases} \dot{M}_{\rm cold} = -\gamma\,\dot{M}_\star, \\ \dot{Z}_{\rm cold} = \dfrac{y_Z(1-\mathcal{R})}{\gamma}\,\dfrac{\dot{M}_{\rm cold}}{M_{\rm cold}}, \end{cases} \tag{52}$$

with initial conditions $M_{\rm cold}(0)=M_{\rm cold,0}$ and $Z_{\rm cold}(0)=0$. The interesting feature of this class of models is that, irrespective of the shape of the SFR $\dot{M}_\star$ and its relation with the gas mass $M_{\rm cold}$, an implicit solution can be provided in terms of the gas mass fraction $\mu\equiv M_{\rm cold}/(M_{\rm cold}+M_\star)$. Solving the above equations in terms of μ, one easily obtains

$$\begin{cases} M_{\rm cold} = M_{\rm cold,0}\,\dfrac{\mu}{\gamma-(\gamma-1)\mu}, \\ Z_{\rm cold} = \dfrac{y_Z(1-\mathcal{R})}{\gamma}\ln\left(\dfrac{1}{\mu}-\dfrac{\gamma-1}{\gamma}\right). \end{cases} \tag{53}$$

At late times, one expects $\mu\ll 1$, and the metallicity asymptotically behaves as $Z_{\rm cold}\simeq y_Z\,(1-\mathcal{R})\gamma^{-1}\ln\mu^{-1}$; this is often referred to as the leaky-box solution. For $\gamma\simeq 1$ (i.e., $\epsilon_{\rm out}=\mathcal{R}=0$), which corresponds to neglecting outflow and recycling, one finds the classical closed-box solution; in such a case, the total mass is constant in time, and hence $\mu\simeq M_{\rm cold}/M_{\rm cold,0}$ and $Z_{\rm cold}\simeq y_Z\ln\mu^{-1}$.

Coming back to the solution in Equation (53), one can find an explicit time dependence by specifying the relation between the SFR and the gas mass; in the way of comparing the outcome with our result of Equations (3) and (9) in the main text, we prescribe as in Equation (1) that $\dot{M}_\star = M_{\rm cold}/\tau_\star = s\,M_{\rm cold}/\tau_{\rm cond}$ and $M_{\rm cold,0}=f_{\rm inf}\,M_b$. In such a case, it is found that

$$\begin{cases} M_{\rm cold}(x) = f_{\rm inf}\,M_b\,e^{-s\gamma\,x}, \\ Z_{\rm cold}(x) = \dfrac{y_Z(1-\mathcal{R})}{\gamma}(s\gamma\,x-\ln\gamma), \end{cases} \tag{54}$$

with $x\equiv\tau/\tau_{\rm cond}$. Clearly, the absence of dilution due to inflow makes the metallicity increase almost linearly with galactic age, while the cold gas reservoir diminishes and gets progressively exhausted. In particular, for the closed-box model ($\gamma\simeq 1$), one has $M_{\rm cold}\propto e^{-s\,\tau/\tau_{\rm cond}}$ and $Z_{\rm cold}\propto y_Z\,\tau/\tau_{\rm cond}$. The evolution of the gas mass and metallicity is illustrated in Figure 12.

A.2. Constant-inflow Models and the Gas-regulator (or Bathtube) Solution

Another class of more realistic analytic models can be obtained when the inflow of gas is assumed to occur at a

constant rate $\dot{M}_{\rm inf}$. The relevant evolution equations read

$$\begin{cases} \dot{M}_{\rm cold} = \dot{M}_{\rm inf} - \gamma\, \dot{M}_{\star}, \\ \dot{Z}_{\rm cold} = -\dfrac{\dot{M}_{\rm inf}}{M_{\rm cold}}\, Z_{\rm cold} + y_Z(1-\mathcal{R})\dfrac{\dot{M}_{\star}}{M_{\rm cold}}, \end{cases} \tag{55}$$

with initial conditions $M_{\rm cold}(0) = Z_{\rm cold}(0) = 0$. To solve the system, a prescription linking the SFR to the gas mass is needed; in the way of comparing with our result, we adopt $\dot{M}_{\star} = M_{\rm cold}/\tau_{\star} = s\, M_{\rm cold}/\tau_{\rm cond}$, as in Equation (1).

The remarkable aspect of the constant-inflow model is that it admits self-consistent steady-state solutions for both the cold gas mass and the cold gas metallicity. In a steady state, the SFR adjusts such that the mass loss due to feedback and mass addition due to inflow exactly compensate, and at the same time, the metal dilution due to inflow and metal production due to star formation also balance. Posing $\dot{M}_{\rm cold} = \dot{Z}_{\rm cold} = 0$ in the equations above, one finds

$$\begin{cases} \bar{M}_{\rm cold} \simeq \dfrac{\dot{M}_{\rm inf}\, \tau_{\rm cond}}{s\gamma}, \\ \bar{Z}_{\rm cold} \simeq \dfrac{y_Z(1-\mathcal{R})}{\gamma}. \end{cases} \tag{56}$$

This steady-state solution is known as the gas-regulator or bathtube model. In the context of galaxy formation, the inflow rate $\dot{M}_{\rm inf}$ is assumed to originate via continuous accretion of gas from the environment outside the host halo; this is reasonable for galaxies that have long star formation timescales like local spirals, while clearly it cannot be retained for high-redshift star-forming galaxies and, specifically, for ETG progenitors.

The steady-state solution is an attractor; i.e., in the long run, the system converges to it. The overall evolution, derived by solving Equation (55), is given by

$$\begin{cases} M_{\rm cold}(x) = \dfrac{f_{\rm inf}\, M_{\rm b}}{s\gamma}\,(1 - e^{-s\gamma\, x}), \\ Z_{\rm cold}(x) = \dfrac{y_Z(1-\mathcal{R})}{\gamma}\left[1 - \dfrac{s\gamma\, x}{e^{s\gamma\, x} - 1}\right], \end{cases} \tag{57}$$

where $x \equiv \tau/\tau_{\rm cond}$, and for easing the comparison with our solutions in Equations (3) and (9), we have prescribed $\dot{M}_{\rm inf} = f_{\rm inf}\, M_{\rm b}/\tau_{\rm cond}$. The evolution of the gas mass and metallicity is illustrated in Figure 12.

ORCID iDs

A. Lapi https://orcid.org/0000-0002-4882-1735

References

Allende Prieto, C., Lambert, D. L., & Asplund, M. 2001, ApJL, 556, L63
Andrews, B. H., Weinberg, D. H., Schonrich, R., & Johnson, J. A. 2017, ApJ, 835, 224
Aoyama, S., Hou, K.-C., Hirashita, H., Nagamine, K., & Shimizu, I. 2018, MNRAS, 478, 4905
Aoyama, S., Hou, K.-C., & Shimizu, I. 2017, MNRAS, 466, 105
Arrigoni, M., Trager, S. C., Somerville, R. S., & Gibson, B. K. 2010, MNRAS, 402, 173
Asano, R. S., Takeuchi, T. T., Hirashita, H., & Inoue, A. K. 2013, EP&S, 65, 213
Athey, A. E., & Bregman, J. N. 2009, ApJ, 696, 681
Aversa, R., Lapi, A., De Zotti, G., Shankar, F., & Danese, L. 2015, ApJ, 810, 74
Barnes, J., & Efstathiou, G. 1987, ApJ, 319, 575
Barro, G., Kriek, M., Pérez-González, P. G., et al. 2016, ApJL, 827, L32
Barro, G., Kriek, M., Perez-Gonzalez, P. G., et al. 2017, ApJL, 851, L40
Behroozi, P. S., Wechsler, R. H., & Conroy, C. 2013, ApJ, 770, 57
Bekki, K. 2013, MNRAS, 436, 2254
Bekki, K. 2015, MNRAS, 449, 1625
Bell, E. F., McIntosh, D. H., Katz, N., & Weinberg, M. D. 2003, ApJS, 149, 289
Benson, A. J. 2012, NewA, 17, 175
Bianchi, S., & Schneider, R. 2007, MNRAS, 378, 973
Bigiel, F., Leroy, A., Walter, F., et al. 2008, AJ, 136, 2846
Bocquet, S., Saro, A., Dolag, K., & Mohr, J. J. 2016, MNRAS, 456, 2361
Boquien, M., Burgarella, D., Roehlly, Y., et al. 2019, A&A, 622, A103
Bouche, N., Dekel, A., Genzel, R., et al. 2010, ApJ, 718, 1001
Bournaud, F. 2016, Galactic Bulges (Switzerland: Springer International Publishing), 355
Bregman, J. N. 1980, ApJ, 365, 544
Bullock, J. S., Dekel, A., Kolatt, T. S., et al. 2001, ApJ, 555, 240
Burkert, A., Forster Schreiber, N. M., Genzel, R., et al. 2016, ApJ, 826, 214
Caon, N., Macchetto, D., & Pastoriza, M. 2000, ApJS, 127, 39
Cassará, L. P., Maccagni, D., Garilli, B., et al. 2016, A&A, 593, A9
Chabrier, G. 2003, ApJL, 586, L133
Chabrier, G. 2005, in The Initial Mass Function 50 years Later, ed. E. Corbelli & F. Palle (Dordrecht: Springer), 41
Chiappini, C., Matteucci, F., & Romano, D. 2001, ApJ, 554, 1044
Chiosi, C. 1980, A&A, 83, 206
Citro, A., Pozzetti, L., Moresco, M., & Cimatti, A. 2016, A&A, 592, A19
Cole, S., Lacey, C. G., Baugh, C. M., & Frenk, C. S. 2000, MNRAS, 319, 168
Collacchioni, F., Cora, S. A., Lagos, C. D. P., & Vega-Martinez, C. A. 2018, MNRAS, 481, 954
Comparat, J., Prada, F., Yepes, G., & Klypin, A. 2017, MNRAS, 469, 4157
Comparat, J., Prada, F., Yepes, G., & Klypin, A. 2019, MNRAS, 483, 2561
Conroy, C. 2013, ARA&A, 51, 393
Cousin, M., Buat, V., Boissier, S., et al. 2016, A&A, 589, A109
Croton, D. J., Springel, V., White, S. D. M., et al. 2006, MNRAS, 365, 11
da Cunha, E., Walter, F., Smail, I. R., et al. 2015, ApJ, 806, 110
Daddi, E., Dickinson, M., Morrison, G., et al. 2007, ApJ, 670, 156
Danovich, M., Dekel, A., Hahn, O., Ceverino, D., & Primack, J. 2015, MNRAS, 449, 2087
Davé, R., Finlator, K., & Oppenheimer, B. D. 2012, MNRAS, 421, 98
de Bennassuti, M., Schneider, R., Valiante, R., & Salvadori, S. 2014, MNRAS, 445, 3039
de los Reyes, M. A., Ly, C., Lee, J. C., et al. 2015, AJ, 149, 79
De Lucia, G., Fontanot, F., & Hirschmann, M. 2017, MNRAS, 466, L88
De Lucia, G., Tornatore, L., Frenk, C. S., et al. 2014, MNRAS, 445, 970
De Rossi, M. E., & Bromm, V. 2019, ApJ, submitted (arXiv:1903.02512)
Dekel, A., Birnboim, Y., Engel, G., et al. 2009, Natur, 457, 451
Dekel, A., Lapiner, S., & Dubois, Y. 2019, A&A, submitted (arXiv:1904.08431)
Dekel, A., & Mandelker, N. 2014, MNRAS, 444, 2071
Draine, B. T. 2003, ARA&A, 41, 241
Draine, B. T. 2011, Physics of the Interstellar and Intergalactic Medium (Princeton, NJ: Princeton Univ. Press)
Dubois, Y., Peirani, S., & Pichon, C. 2016, MNRAS, 463, 3948
Dubois, Y., Pichon, C., Welker, C., et al. 2014, MNRAS, 444, 1453
Dunlop, J. S., McLure, R. J., Biggs, A. D., et al. 2017, MNRAS, 466, 861
Dwek, E. 1998, ApJ, 501, 643
Dwek, E., & Cherchneff, I. 2011, ApJ, 727, 63
Dye, S., Furlanetto, C., Swinbank, A. M., et al. 2015, MNRAS, 452, 2258
Edmunds, M. G. 1990, MNRAS, 246, 678
Elbaz, D., Daddi, E., Le Borgne, D., et al. 2007, A&A, 468, 33
Elmegreen, D. M., Elmegreen, B. G., & Ferguson, T. E. 2005, ApJL, 623, L71
Erb, D. K. 2008, ApJ, 674, 151
Erb, D. K., Shapley, A. E., Pettini, M., et al. 2006, ApJ, 644, 813
Fabian, A. C. 1999, MNRAS, 308, L39
Faisst, A. L., Capak, P. L., Davidzon, I., et al. 2016, ApJ, 822, 29
Fakhouri, O., & Ma, C.-P. 2008, MNRAS, 386, 577
Fakhouri, O., Ma, C.-P., & Boylan-Kolchin, M. 2010, MNRAS, 406, 2267
Feldmann, R. 2015, MNRAS, 449, 3274
Ferrari, F., Pastoriza, M. G., Macchetto, F. D., et al. 2002, A&A, 389, 355
Finlator, K., Oh, S. P., Ozel, F., & Dave, R. 2012, MNRAS, 427, 2464
Fontanot, F., De Lucia, G., Hirschmann, M., et al. 2017, MNRAS, 464, 3812
Forbes, J. C., Krumholz, M. R., Burkert, A., & Dekel, A. 2014a, MNRAS, 443, 168

Forbes, J. C., Krumholz, M. R., Burkert, A., & Dekel, A. 2014b, MNRAS, 438, 1552
Forbes, J. C., Krumholz, M. R., & Speagle, J. S. 2019, MNRAS, 487, 3581
Fu, J., Kauffmann, G., Huang, M.-l., et al. 2013, MNRAS, 434, 1531
Gallazzi, A., Bell, E. F., Zibetti, S., Brinchmann, J., & Kelson, D. D. 2014, ApJ, 788, 72
Gallazzi, A., Charlot, S., Brinchmann, J., & White, S. D. M. 2006, MNRAS, 370, 1106
Genel, S., Bouché, N., Naab, T., Sternberg, A., & Genzel, R. 2010, ApJ, 719, 229
Genel, S., Vogelsberger, M., Springel, V., et al. 2014, MNRAS, 445, 175
Genzel, R., Newman, S., Jones, T., et al. 2011, ApJ, 733, 101
Gioannini, L., Matteucci, F., Vladilo, G., & Calura, F. 2017, MNRAS, 464, 985
Giocoli, C., Tormen, G., & Sheth, R. K. 2012, MNRAS, 422, 185
Granato, G. L., De Zotti, G., Silva, L., Bressan, A., & Danese, L. 2004, ApJ, 600, 580
Greggio, L. 2005, A&A, 441, 1055
Grisoni, V., Spitoni, E., & Matteucci, F. 2018, MNRAS, 481, 2570
Halliday, C., Daddi, E., Cimatti, A., et al. 2008, A&A, 479, 417
Hartwick, F. D. A. 1976, ApJ, 209, 418
Hirashita, H. 2000, PASJ, 52, 585
Hirashita, H., Nozawa, T., Villaume, A., & Srinivasan, S. 2015, MNRAS, 454, 1620
Hirschmann, M., De Lucia, G., & Fontanot, F. 2016, MNRAS, 461, 1760
Hodge, J. A., Swinbank, A. M., Simpson, J. M., et al. 2016, ApJ, 833, 103
Hopkins, P. F., Keres, D., Onorbe, J., et al. 2014, MNRAS, 445, 581
Hopkins, P. F., Quataert, E., & Murray, N. 2012, MNRAS, 421, 3522
Hopkins, P. F., Wetzel, A., Keres, D., et al. 2018, MNRAS, 480, 800
Hudson, M. J., Gillis, B. R., Coupon, J., et al. 2015, MNRAS, 447, 298
Humphrey, P. J., & Buote, D. A. 2006, ApJ, 639, 136
Ikarashi, S., Ivison, R. J., Caputi, K. I., et al. 2015, ApJ, 810, 133
Iliev, I. T., Mellema, G., Shapiro, P. R., & Pen, U.-L. 2007, MNRAS, 376, 534
Imara, N., Loeb, A., Johnson, B. D., Conroy, C., & Behroozi, P. 2018, ApJ, 854, 36
Inoue, A. K. 2003, PASJ, 55, 901
Jiang, F., Dekel, A., Kneller, O., et al. 2019, MNRAS, submitted (arXiv:1804.07306)
Johansson, J., Thomas, D., & Maraston, C. 2012, MNRAS, 421, 1908
Kauffmann, G., White, S. D. M., & Guiderdoni, B. 1993, MNRAS, 264, 201
Kennicutt, R. C., Jr. 1998, ApJ, 498, 541
Kewley, L. J., & Ellison, S. L. 2008, ApJ, 681, 1183
King, A. R. 2003, ApJL, 596, L27
King, A. R. 2014, SSRv, 183, 427
Kitayama, T., & Suto, Y. 1996, MNRAS, 280, 638
Koprowski, M., Dunlop, J. S., Michalowski, M. J., et al. 2016, MNRAS, 458, 4321
Kravtsov, A. V., Vikhlinin, A. A., & Meshcheryakov, A. V. 2018, AstL, 44, 8
Krumholz, M. R., Dekel, A., & McKee, C. F. 2012, ApJ, 745, 69
Kubryk, M., Prantzos, N., & Athanassoula, E. 2015, A&A, 580, A126
Lacey, C., & Cole, S. 1993, MNRAS, 262, 627
Lacey, C. G., Baugh, C. M., Frenk, C. S., et al. 2016, MNRAS, 462, 3854
Lacey, C. G., & Fall, M. 1985, ApJ, 290, 154
Lada, C. J., Lombardi, M., & Alves, J. F. 2010, ApJ, 724, 687
Lagos, C. d. P., Tobar, R. J., Robotham, A. S. G., et al. 2018, MNRAS, 481, 3573
Lang, P., Schinnerer, E., Smail, I., et al. 2019, ApJ, 879, 54
Lapi, A., Mancuso, C., Bressan, A., & Danese, L. 2017, ApJ, 847, 13
Lapi, A., Pantoni, L., Zanisi, L., et al. 2018, ApJ, 857, 22
Lapi, A., Raimundo, S., Aversa, R., et al. 2014, ApJ, 782, 69
Lapi, A., Salucci, P., & Danese, L. 2013, ApJ, 772, 85
Lapi, A., Shankar, F., Mao, J., et al. 2006, ApJ, 650, 42
Lara-Lopez, M. A., Lopez-Sanchez, Á. R., & Hopkins, A. M. 2013, ApJ, 764, 178
Lilly, S. J., Carollo, C. M., Pipino, A., Renzini, A., & Peng, Y. 2013, ApJ, 772, 119
Loewenstein, M., & Mathews, W. G. 1991, ApJ, 373, 445
Ma, J., Gonzalez, A. H., Viera, J. D., et al. 2016, ApJ, 832, 114
Mac Low, M.-M., & Ferrara, A. 1999, ApJ, 513, 142
Macció, A. V., Dutton, A. A., van den Bosch, F. C., et al. 2007, MNRAS, 378, 55
Maiolino, R., Cox, P., Caselli, P., et al. 2005, A&A, 440, L51
Maiolino, R., & Mannucci, F. 2019, A&ARv, 27, 3
Maiolino, R., Nagao, T., Grazian, A., et al. 2008, A&A, 488, 463
Man, A. W. S., Greve, T. R., Toft, S., et al. 2016, ApJ, 820, 11
Mancini, M., Schneider, R., Graziani, L., et al. 2015, MNRAS, 451, L70
Mancuso, C., Lapi, A., Shi, J., et al. 2016a, ApJ, 823, 128
Mancuso, C., Lapi, A., Shi, J., et al. 2016b, ApJ, 833, 152
Mandelbaum, R., Wang, W., Zu, Y., et al. 2016, MNRAS, 457, 3200
Mannucci, F., Cresci, G., Maiolino, R., Marconi, A., & Gnerucci, A. 2010, MNRAS, 408, 2115
Mannucci, F., Della Valle, M., & Panagia, N. 2006, MNRAS, 370, 773
Maoz, D., & Graur, O. 2017, ApJ, 848, 25
Maoz, D., Mannucci, F., & Nelemans, G. 2014, ARA&A, 52, 107
Marconi, G., Matteucci, F., & Tosi, M. 1994, MNRAS, 270, 35
Mathews, W. G., & Brighenti, F. 2003, ARA&A, 41, 191
Matteucci, F. 2012, Chemical Evolution of Galaxies (Berlin: Springer)
Matteucci, F., & Chiosi, C. 1983, A&A, 123, 121
Matteucci, F., & Greggio, L. 1986, A&A, 154, 279
McAlpine, S., Helly, J. C., Schaller, M., et al. 2016, A&C, 15, 72
McAlpine, S., Smail, I., Bower, R. G., et al. 2019, MNRAS, 488, 2440
McKee, C. 1989, in Proc. IAU Symp. 135, Interstellar Dust, ed. L. J. Allamandola & A. G. G. M. Tielens (Dordrecht: Kluwer), 431
McKinnon, R., Torrey, P., Vogelsberger, M., Hayward, C. C., & Marinacci, F. 2017, MNRAS, 468, 1505
McKinnon, R., Vogelsberger, M., Torrey, P., Marinacci, F., & Kannan, R. 2018, MNRAS, 478, 2851
Michalowski, M. J. 2015, A&A, 577, A80
Mo, H., van den Bosch, F., & White, S. D. M. 2010, Galaxy Formation and Evolution (Cambridge: Cambridge Univ. Press)
Mo, H. J., & Mao, S. 2004, MNRAS, 353, 829
Mollá, M., Cavichia, O., Gavilan, M., & Gibson, B. K. 2015, MNRAS, 451, 3693
More, S., van den Bosch, F. C., Cacciato, M., et al. 2011, MNRAS, 410, 210
Moreno, J., Giocoli, C., & Sheth, R. K. 2009, MNRAS, 397, 299
Moster, B. P., Naab, T., & White, S. D. M. 2013, MNRAS, 428, 3121
Moustakas, J., Coil, A. L., Aird, J., et al. 2013, ApJ, 767, 50
Murray, N., Quataert, E., & Thompson, T. A. 2005, ApJ, 618, 569
Naab, T., & Ostriker, J. P. 2006, MNRAS, 366, 899
Naab, T., & Ostriker, J. P. 2017, ARA&A, 55, 59
Navarro, J. F., Frenk, C. S., & White, S. D. M. 1997, ApJ, 490, 493
Negrello, M., Hopwood, R., Dye, S., et al. 2014, MNRAS, 440, 1999
Noeske, K. G., Weiner, B. J., Faber, S. M., et al. 2007, ApJL, 660, L43
Nomoto, K., Kobayashi, C., & Tominaga, N. 2013, ARA&A, 51, 457
Omont, A., Willott, C. J., Beelen, A., et al. 2013, A&A, 552, A43
Onodera, M., Carollo, C. M., Lilly, S., et al. 2016, ApJ, 822, 42
Oppenheimer, B. D., & Dave, R. 2006, MNRAS, 373, 1265
Pagel, B. E. J., & Patchett, B. E. 1975, MNRAS, 172, 13
Pallottini, A., Ferrara, A., Gallerani, S., et al. 2017, MNRAS, 465, 2540
Papovich, C., Finkelstein, S. L., Ferguson, H. C., Lotz, J. M., & Giavalisco, M. 2011, MNRAS, 412, 1123
Pawlik, A. H., Schaye, J., & van Scherpenzeel, E. 2009, MNRAS, 394, 1812
Pezzulli, G., & Fraternali, F. 2016, AN, 337, 913
Pilyugin, L. S. 1993, A&A, 277, 42
Pipino, A., Lilly, S. J., & Carollo, C. M. 2014, MNRAS, 441, 1444
Pitts, E., & Tayler, R. J. 1989, MNRAS, 240, 373
Planck Collaboration 2018, ApJ, in press (arXiv:1807.06209)
Popesso, P., Concas, A., Morselli, L., et al. 2019, MNRAS, 483, 3213
Popping, G., Somerville, R. S., & Galametz, M. 2017, MNRAS, 471, 3152
Porter, L. A., Somerville, R. S., Primack, J. R., et al. 2014, MNRAS, 445, 3092
Recchi, S., & Kroupa, P. 2015, MNRAS, 446, 4168
Recchi, S., Spitoni, E., Matteucci, F., & Lanfranchi, G. A. 2008, A&A, 489, 555
Remy-Ruyer, A., Madden, S. C., Galliano, F., et al. 2014, A&A, 563, A31
Renzini, A. 2006, ARA&A, 44, 141
Renzini, A., & Peng, Y.-J. 2015, ApJL, 801, L29
Ricarte, A., Tremmel, M., Natarajan, P., et al. 2019, MNRAS, submitted (arXiv:1904.10116)
Rodighiero, G., Brusa, M., Daddi, E., et al. 2015, ApJL, 800, L10
Rodighiero, G., Daddi, E., Baronchelli, I., et al. 2011, ApJL, 739, L40
Rodriguez-Gomez, V., Genel, S., Vogelsberger, M., et al. 2015, MNRAS, 449, 49
Rodriguez-Gomez, V., Pillepich, A., Sales, L. V., et al. 2016, MNRAS, 458, 2371
Rodriguez-Puebla, A., Avila-Reese, V., Yang, X., et al. 2015, ApJ, 799, 130
Rodriguez-Puebla, A., Primack, J. R., Behroozi, P., & Faber, S. M. 2016, MNRAS, 455, 2592
Romano, D., Karakas, A. I., Tosi, M., & Matteucci, F. 2010, A&A, 522, A32
Saintonge, A., Catinella, B., Tacconi, L. J., et al. 2017, ApJS, 233, 22
Sanders, R. L., Shapley, A. E., Kriek, M., et al. 2015, ApJ, 799, 138
Santini, P., Maiolino, R., Magnelli, B., et al. 2014, A&A, 562, A30
Schaye, J., Crain, R. A., Bower, R. G., et al. 2015, MNRAS, 446, 521

Schmidt, M. 1959, ApJ, 129, 243
Schmidt, M. 1963, ApJ, 137, 758
Schonrich, R., & Binney, J. 2009, MNRAS, 396, 203
Schreiber, C., Pannella, M., Leiton, R., et al. 2017, A&A, 599, A134
Scoville, N., Aussel, H., Sheth, K., et al. 2014, ApJ, 783, 84
Scoville, N., Lee, N., Vanden Bout, P., et al. 2017, ApJ, 837, 150
Scoville, N., Sheth, K., Aussel, H., et al. 2016, ApJ, 820, 83
Shankar, F., Lapi, A., Salucci, P., de Zotti, G., & Danese, L. 2006, ApJ, 643, 14
Shi, J., Lapi, A., Mancuso, C., Wang, H., & Danese, L. 2017, ApJ, 843, 105
Shull, J. M., Harness, A., Trenti, M., & Smith, B. D. 2012, ApJ, 747, 100
Silk, J., & Mamon, G. A. 2012, RAA, 12, 917
Silk, J., & Rees, M. J. 1998, A&A, 331, L1
Simpson, J. M., Smail, I., Swinbank, A. M., et al. 2015, ApJ, 807, 128
Somerville, R. S., & Dave, R. 2015, ARA&A, 53, 51
Somerville, R. S., Hopkins, P. F., & Cox, T. J. 2008, MNRAS, 391, 481
Sommariva, V., Mannucci, F., Cresci, G., et al. 2012, A&A, 539, A136
Speagle, J. S., Steinhardt, C. L., Capak, P. L., & Silverman, J. 2014, ApJS, 214, 15
Spilker, J. S., Marrone, D. P., Aravena, M., et al. 2016, ApJ, 826, 112
Spitoni, E., Matteucci, F., & Marcon-Uchida, M. M. 2013, A&A, 551, A123
Spitoni, E., Recchi, S., & Matteucci, F. 2008, A&A, 484, 743
Spitoni, E., Romano, D., Matteucci, F., & Ciotti, L. 2015, ApJ, 802, 129
Spitoni, E., Vincenzo, F., & Matteucci, F. 2017, A&A, 599, A6
Springel, V., Pakmor, R., Pillepich, A., et al. 2018, MNRAS, 475, 676
Steidel, C. C., Rudie, G. C., Strom, A. L., et al. 2014, ApJ, 795, 165
Steinhardt, C. L., Speagle, J. S., & Capak, P. 2014, ApJL, 791, L25
Stevens, A. R. H., & Brown, T. 2017, MNRAS, 471, 447
Stevens, A. R. H., Croton, D. J., & Mutch, S. J. 2016, MNRAS, 461, 859
Stevens, A. R. H., Lagos, C. d. P., Obreschkow, D., & Sinha, M. 2018, MNRAS, 481, 5543
Straatman, C. M. S., Labbe, I., & Spitler, L. R. 2015, ApJL, 808, L29
Sutherland, R. S., & Dopita, M. A. 1993, ApJS, 88, 253
Suzuki, T. L., Kodama, T., Onodera, M., et al. 2017, ApJ, 849, 39
Tacchella, S., Bose, S., Conroy, C., Eisenstein, D. J., & Johnson, B. D. 2018a, ApJ, 868, 92
Tacchella, S., Carollo, C. M., Forster Schreiber, N. M., et al. 2018b, ApJ, 859, 56
Tacconi, L. J., Genzel, R., Saintonge, A., et al. 2018, ApJ, 853, 179
Tadaki, K.-I., Genzel, R., Kodama, T., et al. 2017a, ApJ, 834, 135
Tadaki, K.-I., Kodama, T., Nelson, E. J., et al. 2017b, ApJL, 841, L25
Talbot, R. J., Jr., & Arnett, W. D. 1971, ApJ, 170, 409
Talia, M., Pozzi, F., Vallini, L., et al. 2018, MNRAS, 476, 3956
Thomas, D., Maraston, C., Bender, R., & Mendes de Oliveira, C. 2005, ApJ, 621, 673
Thomas, D., Maraston, C., Schawinski, K., Sarzi, M., & Silk, J. 2010, MNRAS, 404, 1775
Tinker, J., Kravtsov, A. V., Klypin, A., et al. 2008, ApJ, 688, 709
Tinsley, B. M. 1974, ApJ, 192, 629
Torrey, P., Vogelsberger, M., Marinacci, F., et al. 2019, MNRAS, 484, 5587
Totani, T., Morokuma, T., Oda, T., Doi, M., & Yasuda, N. 2008, PASJ, 60, 1327
Tremonti, C. A., Heckman, T. M., Kauffmann, G., et al. 2004, ApJ, 613, 898
Valiante, R., Schneider, R., Bianchi, S., & Andersen, A. C. 2009, MNRAS, 397, 1661
Velander, M., van Uitert, E., Hoekstra, H., et al. 2014, MNRAS, 437, 2111
Venemans, B. P., Decarli, R., Walter, F., et al. 2018, ApJ, 866, 159
Vincenzo, F., Matteucci, F., Belfiore, F., & Maiolino, R. 2016, MNRAS, 455, 4183
Vincenzo, F., Matteucci, F., & Spitoni, E. 2017, MNRAS, 466, 2939
Vogelsberger, M., Genel, S., Springel, V., et al. 2014, MNRAS, 444, 1518
Walcher, C. J., Yates, R. M., Minchev, I., et al. 2016, A&A, 594, A61
Wang, R., Carilli, C. L., Wagg, J., et al. 2008, ApJ, 687, 848
Watson, W. A., Iliev, I. T., D'Aloisio, A., et al. 2013, MNRAS, 433, 1230
Weinberg, D. H., Andrews, B. H., & Freudenburg, J. 2017, ApJ, 837, 183
Whitaker, K. E., Franx, M., Leja, J., et al. 2014, ApJ, 795, 104
White, S. D. M., & Frenk, C. S. 1991, ApJ, 379, 52
Willott, C. J., Bergeron, J., & Omont, A. 2015, ApJ, 801, 123
Wojtak, R., & Mamon, G. A. 2013, MNRAS, 428, 2407
Zahid, H. J., Kashino, D., Silverman, J. D., et al. 2014, ApJ, 792, 75
Zhao, D. H., Mo, H. J., Jing, Y. P., & Borner, G. 2003, MNRAS, 339, 12
Zhukovska, S., Dobbs, C., Jenkins, E. B., & Klessen, R. S. 2016, ApJ, 831, 147
Zhukovska, S., Gail, H.-P., & Trieloff, M. 2008, A&A, 479, 453
Zjupa, J., & Springel, V. 2017, MNRAS, 466, 1625
Zolotov, A., Dekel, A., Mandelker, N., & Tweed, D. 2015, MNRAS, 450, 2327